JGR Atmospheres

RESEARCH ARTICLE
10.1029/2022JD037817

Intercomparison of Atmospheric Carbonyl Sulfide (TransCom-COS; Part One): Evaluating the Impact of Transport and Emissions on Tropospheric Variability Using Ground-Based and Aircraft Data

Marine Remaud[1], Jin Ma[2], Maarten Krol[2,3], Camille Abadie[1], Michael P. Cartwright[4,5], Prabir Patra[6], Yosuke Niwa[7,8], Christian Rodenbeck[9], Sauveur Belviso[1], Linda Kooijmans[3], Sinikka Lennartz[10], Fabienne Maignan[1], Frédéric Chevallier[1], Martyn P. Chipperfield[11,12], Richard J. Pope[11,12], Jeremy J. Harrison[4,5], Isaac Vimont[13], Christopher Wilson[11,12], and Philippe Peylin[1]

[1]Laboratoire des Sciences du Climat et de l'Environnement, CEA-CNRS-UVSQ, UMR 8212, IPSL, Gif-sur-Yvette, France, [2]Institute for Marine and Atmospheric Research, Utrecht University, Utrecht, The Netherlands, [3]Meteorology and Air Quality, Wageningen University and Research, Wageningen, The Netherlands, [4]School of Physics and Astronomy, Space Park Leicester, University of Leicester, Leicester, UK, [5]National Centre for Earth Observation, Space Park Leicester, University of Leicester, Leicester, UK, [6]Research Institute for Global Change, JAMSTEC, Yokohama, Japan, [7]National Institute for Environmental Studies, Tsukuba, Ibaraki, Japan, [8]Meteorological Research Institute, Tsukuba, Ibaraki, Japan, [9]Max Planck Institute for Biogeochemistry, Jena, Germany, [10]Institute for Chemistry and Biology of the Marine Environment, University of Oldenburg, Oldenburg, Germany, [11]School of Earth and Environment, University of Leeds, Leeds, UK, [12]National Centre for Earth Observation, University of Leeds, Leeds, UK, [13]National Oceanic and Atmospheric Administration, Boulder, CO, USA

Abstract We present a comparison of atmospheric transport model (ATM) simulations for carbonyl sulfide (COS), within the framework of the atmospheric tracer transport model intercomparison project "TransCom-COS." Seven ATMs participated in the experiment and provided simulations of COS mixing ratios over the years 2010–2018, using state-of-the-art surface fluxes for various components of the COS budget: biospheric sink, oceanic source, sources from fire and industry. The main goal of TransCom-COS is to investigate the impact of the transport uncertainty and emission distribution in simulating the spatio-temporal variability of tropospheric COS mixing ratios. A control case with seasonal surface fluxes of COS was constructed. The results indicate that the COS mixing ratios are underestimated by at least 50 parts per trillion (ppt) in the tropics, pointing to a missing tropical source. In summer, the mixing ratios are overestimated by at least 50 ppt above 40°N, pointing to a likely missing sink in the high northern latitudes. Regarding the latitudinal profile, the model spread is greater than 60 ppt above 40°N in boreal summer. Regarding the seasonal amplitude, the model spread reaches 50 ppt at 6 out of 15 sites, compared to an observed seasonal amplitude of 100 ppt. All models simulated a too late minimum by at least 2–3 months at two high northern-latitude sites, likely owing to errors in the seasonal cycle in the ocean emissions. This study highlighted the shortcomings in the COS global budget that need to be resolved before using COS as a photosynthesis tracer.

Plain Language Summary In this study, we evaluate the state-of-the-art fluxes for various components of the carbonyl sulfide (COS) budget: biospheric sink, oceanic source, sources from fire and industry. A control case with seasonal surface fluxes of COS was constructed. Seven atmospheric transport models provided simulations of COS mixing ratios. Then, the simulated mixing ratios were evaluated against atmospheric measurements at several surface sites. Results show that all models fail to capture the observed latitudinal distribution and that the model spread is small compared to the model-observation mismatch. In summer, the overestimated mixing ratios above 40°N point to a likely missing sink in the high northern latitudes. The underestimated mixing ratios in the tropics point to a missing tropical source. This study highlighted the shortcomings in the COS global budget that need to be resolved before using COS as a photosynthesis tracer.

Key Points:

- The model-observation mismatch suggests there is a missing source in the tropics and a missing sink in the high northern latitude in summer
- At northern latitude sites, the model spread in seasonal amplitude reaches 50 ppt compared to a mean seasonal amplitude of about 100 ppt
- The diurnal rectifier effect is small, decreasing the seasonal amplitude by up to 20% at continental sites

Supporting Information:

Supporting Information may be found in the online version of this article.

Correspondence to:

M. Remaud,
marine.remaud@lsce.ipsl.fr

Citation:

Remaud, M., Ma, J., Krol, M., Abadie, C., Cartwright, M. P., Patra, P., et al. (2023). Intercomparison of atmospheric carbonyl sulfide (TransCom-COS; part one): Evaluating the impact of transport and emissions on tropospheric variability using ground-based and aircraft data. *Journal of Geophysical Research: Atmospheres*, *128*, e2022JD037817. https://doi.org/10.1029/2022JD037817

Received 7 SEP 2022
Accepted 21 FEB 2023
Corrected 10 APR 2023

This article was corrected on 10 APR 2023. See the end of the full text for details.

Author Contributions:

Conceptualization: Marine Remaud, Jin Ma, Maarten Krol, Philippe Peylin

Data curation: Marine Remaud, Jin Ma, Camille Abadie, Michael P. Cartwright, Prabir Patra, Yosuke Niwa, Christian Rodenbeck, Sauveur Belviso, Linda Kooijmans, Sinikka Lennartz, Fabienne Maignan, Isaac Vimont
Formal analysis: Marine Remaud, Jin Ma, Maarten Krol, Philippe Peylin
Funding acquisition: Frédéric Chevallier
Methodology: Marine Remaud, Maarten Krol, Philippe Peylin
Project Administration: Philippe Peylin
Software: Michael P. Cartwright, Prabir Patra, Yosuke Niwa, Christian Rodenbeck, Sauveur Belviso, Martyn P. Chipperfield, Richard J. Pope, Jeremy J. Harrison, Christopher Wilson
Supervision: Maarten Krol, Philippe Peylin
Writing – original draft: Marine Remaud, Maarten Krol
Writing – review & editing: Marine Remaud, Jin Ma, Maarten Krol, Camille Abadie, Michael P. Cartwright, Prabir Patra, Yosuke Niwa, Christian Rodenbeck, Sauveur Belviso, Linda Kooijmans, Sinikka Lennartz, Fabienne Maignan, Frédéric Chevallier, Martyn P. Chipperfield, Richard J. Pope, Jeremy J. Harrison, Isaac Vimont, Christopher Wilson, Philippe Peylin

1. Introduction

Carbonyl sulfide (COS) is a rather long-lived sulfur-containing trace gas with a mean atmospheric mixing ratio less than 500 parts per trillion (ppt). Due to its long lifetime (~2.5 yr), COS reaches the stratosphere, where its decay products contribute to the formation of Stratospheric Sulfur Aerosol. COS is emitted directly and indirectly by the ocean and industrial activities, directly from biomass burning and anoxic soils (Whelan et al., 2018). The main sink of COS is the uptake by the terrestrial biosphere (Berry et al., 2013; Blake et al., 2008; Campbell et al., 2008; Montzka et al., 2007; Suntharalingam et al., 2008), with minor sink contributions also from photochemical oxidation in the troposphere and stratosphere (Whelan et al., 2018). COS is taken up in leaves through similar pathways as carbon dioxide, but without significant respiration (Protoschill-Krebs et al., 1996; Wohlfahrt et al., 2012). For this reason, COS has been proposed as a tracer that can be used to infer Gross Primary Productivity (GPP) at large scale (Campbell et al., 2008; Hu et al., 2021; Le Kuai et al., 2022; Montzka et al., 2007; Remaud et al., 2022).

To infer GPP from COS we need several pieces of information that are currently still highly uncertain. Indeed, the current flux estimates do not lead to a closed COS budget that would be in line with the near-constant COS burden in the atmosphere from 2000 up to 2015 (Whelan et al., 2018). Several studies suggest that sources are missing from the tropical oceans (Berry et al., 2013; Glatthor et al., 2015; Kuai et al., 2015; Launois et al., 2015; Remaud et al., 2022), but currently no hard evidence has been obtained from shipboard measurements (Lennartz et al., 2017, 2020, 2021). Recent inverse modeling studies (Ma et al., 2021; Remaud et al., 2022) confirm the need for a tropical source of COS (or a reduced tropical sink) and more COS uptake at high northern latitudes. Interestingly, while the results of Ma et al. (2021) point to too low modeled COS mixing ratios in the free troposphere, Remaud et al. (2022) could not confirm this finding. This discrepancy triggers the question of how well atmospheric transport models (ATMs) are able to simulate the global COS distribution. Since the source-sink distribution of COS is distinctly different from that of CO_2, a COS model comparison may lead to additional information relative to earlier comparisons that were conducted within the atmospheric tracer transport model intercomparison project TransCom (Gurney et al., 2002; Law et al., 1996). For instance, the one-way uptake of COS by the biosphere both during day and night (Kooijmans et al., 2021; Maignan et al., 2021) differs from the CO_2 interaction with the biosphere with respiration at night and uptake dominating during daytime. On larger scales, the seasonal cycle of COS shows strong signs of biosphere uptake in the Northern Hemisphere (NH) summer and ocean emissions in the Southern Hemisphere (SH; Montzka et al., 2007). As a result, the gradient between the NH and SH changes seasonally, and in a different way than the CO_2 gradient.

It is however important to realize that the various terms in the COS budget are currently still very uncertain. It is therefore important to study the behavior of various surface flux terms in a variety of models, to investigate whether different models point to similar inconsistencies in the global COS budget. The aim of this paper (and a complementary paper, part 2) is to analyze results from a model intercomparison study that focuses on COS. Specifically, we address the questions.

1. What are the comparative roles of uncertainties in transport versus emission distribution in simulating the interhemispheric (IH) gradient, seasonal cycle, and vertical profiles of COS?
2. How large is the model-to-model spread compared to the mismatch between the model and observations (i.e., how sure are we that there is something wrong with the fluxes)?
3. What is the sensitivity of simulated tropospheric COS mixing ratios to the diurnal variability in COS biosphere fluxes?

The third question has been addressed before in TransCom for CO_2 simulations, and is commonly referred to as a (diurnal) rectifier effect (Denning et al., 1995, 1999). Simply said, the question addresses the issue whether the use of monthly mean biosphere fluxes is sufficient to reliably simulate the COS tropospheric seasonal cycle, or should the biosphere be resolved on higher time resolution?

To answer these questions the paper is structured as follows: Section 2 describes the modeling protocol, the participating models, and the measurements that were used to evaluate the models, Section 3 presents the results, and Section 4 ends with a discussion and our conclusions. The paper is the part one of the "Transcom-COS" experiment and focuses on model simulations using the state-of-the-art bottom-up fluxes. Part two of "Transcom-COS" will be the subject of a second paper focused on the two sets of fluxes (Ma et al., 2021; Remaud et al., 2022) that were optimized using atmospheric surface observations.

Table 1
Main Characteristics (Vertical Resolution, Horizontal Resolution, Meteorological Drivers, Transport and Sub-Grid Parameterization Schemes) of the TransCom Models Used in This Experiment

Transport model	Meteorology	Horizontal and vertical resolutions	Reference	Convection scheme	PBL mixing scheme	Advection scheme
LMDz	Nudging toward horizontal winds from ERA-5	1.875° × 3.75°, 39η	Remaud et al. (2018)	Emanuel (1991) and Rochetin et al. (2013)	Small-scale turbulence: Mellor and Yamada (1974); shallow convection: Rio and Hourdin (2008)	Hourdin and Armengaud (1999) and Leer (1997)
TM5	Meteo-and surface fields from ERA-Interim	2° × 2°, 25η	Krol et al. (2005)	Convective mass fluxes from ERA-Interim	Near-surface mixing: Louis (1979); free troposphere mixing: Holtslag and Moeng (1991)	Slopes advection scheme: Russell and Lerner (1981)
TM3	Meteo-and surface fields from NCEP	4° × 5°, 19η	Heimann et al. (2003)	Tiedtke (1989)	Louis (1979)	Slopes advection scheme: Russell and Lerner (1981)
TOMCAT	Forced with the surface pressure, vorticity, divergence from ERA-Interim	2.8° × 2.8°, 60η (surface to ~60 km)	Chipperfield (2006)	Convective mass fluxes from ERA-Interim	Louis (1979)	Prather (1986)
MIROC4	Nudging toward horizontal winds and temperature from JRA-55	T42 spectral truncation (~2.8° × 2.8°), 67η	Patra et al. (2018)	Arakawa and Schubert (1974), with updates	Mellor and Yamada (1982)	S.-J. Lin and Rood (1996)
NICAM5	Nudging toward horizontal winds from JRA-55	~223 km (icosahedral grid), 40z*	Niwa et al. (2017)	Chikira and Sugiyama (2010)	MYNN (Mellor & Yamada, 1974; Nakanishi & Niino, 2004) Level 2 scheme	Miura (2007) and Niwa et al. (2011)
NICAM6	Nudging toward horizontal winds from JRA-55	~112 km (icosahedral grid), 40z*	Niwa et al. (2017)	Chikira and Sugiyama (2010)	MYNN (Mellor & Yamada, 1974; Nakanishi & Niino, 2004) Level 2 scheme	Miura (2007) and Niwa et al. (2011)

Note. η vertical coordinates are a hybrid sigma-pressure coordinate and z^* is the terrain-following vertical coordinate based on the geometric height.

2. Participating Models and Outputs

2.1. Participating Models and Outputs

Seven ATMs participated in the intercomparison of modeled COS mixing ratios. These models represent the diversity existing in the research community. The main features of each transport model, that is, the horizontal and vertical resolution, meteorological drivers are given in Table 1. Almost all models use meteorological fields from atmospheric reanalysis (ERA5, ERA-Interim, NCEP, and JRA-55), either by direct use, or by nudging toward fields of horizontal winds (e.g., LMDz; MIROC4). The TOMCAT ATM is forced by fields of surface pressure, vorticity, and divergence from ERA-Interim. For this model and TM5, the convective mass fluxes are taken from ERA-Interim and averaged to the model grid, which has a coarser resolution than ERA-Interim. In terms of resolution, NICAM6 has the highest horizontal resolution (~1°) while the TM3 ATM has the coarsest resolution (~5° × 4°).

The vertical mixing in the convective boundary layer is represented with different parameterizations in the different models. For deep convective mixing, parameterizations rely on the mass-flux approach and are mainly adapted from three convective schemes: the Arakawa and Schubert (1974) scheme (MIROC4, NICAM 5&6), the Tiedtke (1989) scheme (TM3) and the Emanuel (1991) scheme (LMDz). The convective mass fluxes from ERA-Interim given to the TOMCAT and TM5 ATMs are based on a modified version of the Tiedtke (1989) scheme in the European Center for Medium-Range Weather Forecasts (ECMWF)'s Integrated Forecasting System (Bechtold et al., 2014). The Arakawa and Schubert (1974) scheme spectrally represents multiple cloud types with

different cloud base mass fluxes. The Tiedtke (1989) scheme is a single plume entraining-detraining model. The Emanuel (1991) convective scheme, implemented in LMDz, represents an ensemble of cumulus by an undiluted updraft and a spectrum of mixtures with the environmental air. The subgrid-scale parameterization schemes are also referenced in Table 1, although most of them have been modified from their original formulations. In most of them, the sensitivity of the convective development to environmental humidity has been enhanced either by setting up a threshold based on relative humidity to prevent deep convection from triggering too often (MIROC4, Patra et al., 2018) or by increasing the entrainment of air from the environment in the mixtures (LMDz, Grandpeix et al., 2004) or in the plume (NICAM, Chikira & Sugiyama, 2010) when the environment is too dry. In LMDz, the convective triggering is now based on sub-cloud-scale processes and no longer on the Convective Available Potential Energy (CAPE), improving the diurnal cycle of convection (Rio & Hourdin, 2008).

Simulations were performed using meteorology and surface emissions for the period from 2010 to 2018. The first 2 yr are considered as spin-up and therefore not included in the analysis. As this study focuses on the spatio-temporal COS variability and the COS budget is currently not closed (see Table 3), we do not attempt to reproduce the observed mean COS values and the simulations started from a null initial state. For simplicity, oxidation within the troposphere, estimated as 100 GgS.yr^{-1}, photolysis in the stratosphere, estimated as 35–60 GgS.yr^{-1}, have not been considered, enabling us to isolate the influence of transport processes on COS tropospheric variability. The impact of the COS chemical loss through OH oxidation and photolysis are discussed in the second paper of this model intercomparison. Results (not shown) indicate that including the COS chemistry does not resolve the poor model-observation mismatch.

Model output was generated at each measurement time and location used in the analysis as an hourly average. Modelers chose the horizontal positions to report simulated concentrations; either from a nearest grid point value, or interpolated to the site location from values at surrounding grid points. Additionally, 3-D fields of monthly mean COS mixing ratios were stored and analyzed. Higher temporal resolutions were not considered since this study only examines seasonal and longer timescales, and to prevent excessively large file sizes. A more complete description of each ATM is given in Annex A.

2.2. Prescribed Flux Components

The prescribed COS flux components used as model inputs are presented in Table 2. Each participating group interpolated the emissions horizontally in space to their (coarser) model grid, while ensuring mass conservation. Subsequently, the fluxes provided lower boundary conditions of each ATM, which then simulates the transport of COS by the atmospheric flow. Relying on the linearity of the atmospheric transport, each flux of each scenario was transported separately by all participating models, and the various concentration contributions of the individual fluxes were then added for different scenarios (i.e., combination of fluxes) as described in Section 2.4.

The biosphere fluxes BIO_SIB4 and BIO_ORC, simulated by the SIB4 Land Surface Model (LSM; Kooijmans et al., 2021) and the ORCHIDEE LSM (Abadie et al., 2022; Maignan et al., 2021), respectively, include the COS absorption by vegetation and the net absorption by oxic soils. In both LSMs, the absorption by vegetation is parameterized following the formulation of Berry et al. (2013) as a series of three conductances from the leaf boundary layer to the site of COS hydrolysis in the mesophyll cells. These conductances include the conductance from canopy air to the leaf surface or boundary layer conductance, the stomatal conductance and the internal conductance. The boundary layer conductance is considered to be much larger than the two others conductances. The internal conductance combines the diffusion of COS to the mesophyll cells and the efficiency of the leaf mesophyll carbonic anhydrase (CA) to hydrolyze COS. It is scaled to the maximum rate of the Rubisco enzyme with two scaling factors determined experimentally by Berry et al. (2013) for the two photosynthetic pathways C_3 and C_4. In the SIB4 and ORCHIDEE LSM, the Berry et al. (2013) model was adapted to represent the COS absorption at night that arises from incomplete stomatal closure (Kooijmans et al., 2021; Maignan et al., 2021). The COS plant uptake was rescaled using a monthly climatology of spatially varying COS surface mixing ratios. The latter were obtained by transporting the optimized COS fluxes from Ma et al. (2021) with the TM5 ATM.

The soil fluxes include the COS irreversible uptake via hydrolysis and an abiotic production term. The COS uptake is parameterized with the Ogee et al. (2016) model which represents the abiotic hydrolysis of COS in soil water and the biotic hydrolysis of COS catalyzed by soil micro-organism. The latter, the dominant term, is parameterized using for each biome a CA enhancement factor which characterizes the soil microbial community that

Table 2
Prescribed Carbonyl Sulfide Surface Fluxes Used as Model Input

Process	Name	Time resolution	Spatial resolution	Period	Reference	Total global flux (GgS.yr−1)
Vegetation + soil from SIB4	BIO_SIB4	Monthly, interannual	1° × 1°	2010–2018: monthly fluxes	Kooijmans et al. (2021)	−669 (vegetation) −91 (soil)
Vegetation + soil from SIB4	BIO_SIB4_Diurnal	3-hourly	1° × 1°	2015: 3-hourly fluxes	Kooijmans et al. (2021)	−654 (vegetation) −92 (soil)
Vegetation + soil from ORCHIDEE	BIO_ORC	Monthly, interannual, 3-hourly	0.5° × 0.5°	2010–2018: monthly fluxes, 2015: 3-hourly fluxes	Abadie et al. (2022) and Maignan et al. (2021)	−531 (vegetation) −264 (soil)
Biomass burning	BB	Monthly, interannual	1° × 1°	2010–2016	Stinecipher et al. (2019)	+53
Anthropogenic	ANT	Monthly, interannual	1° × 1°	2010–2015	Zumkehr et al. (2018)	+397
Direct oceanic emissions + indirect emissions from CS_2	OCE	Monthly, interannual	T42 grid (ca. 2.8° × 2.8°)	2010–2018	Lennartz et al. (2017, 2020)	+203
Indirect oceanic emission via DMS	OCE_DMS	Monthly, interannual	T42 grid (ca. 2.8° × 2.8°)	Climatological	Lana et al. (2012) and Lennartz et al. (2017)	+70
Indirect oceanic emissions via DMS from NEMO PISCES	OCE_DMS_PISCES	Monthly, climatological	91 × 144 (2° × 2.5°)	Climatological	Belviso et al. (2012)	+119

Note. Mean magnitudes of the fluxes are given in GgS.yr^{-1} for the period 2010–2018.

can consume COS. The enhancement factors were taken from Meredith et al. (2019) and adapted to the biomes of ORCHIDEE and SIB4. The abiotic production term represents the production due to abiotic thermal degradation and photodegradation of soil organic matter. In the ORCHIDEE LSM, the abiotic term is parameterized following the approach described in Whelan et al. (2016) while, in the SIB4 LSM, it is based on Meredith et al. (2018). The abiotic production of COS increases exponentially with temperature. The emissions from anoxic soils are not considered in this study because of the absence of reliable emission estimates at the beginning of this study. Combining the wetland map of Tootchi et al. (2019) with the temperature-dependent model of Ogee et al. (2016), Abadie and Maignan(2022) recently estimated that anoxic soils emit around 100 GgS.yr^{-1} globally, mainly in the tropics. Their impact on the IH gradient and the seasonal cycle of COS mixing ratio at the NOAA surface stations have been shown to be negligible and, therefore, their inclusion will not affect the conclusion of this study. However, the impact of anoxic soils on the seasonal cycle could be underestimated as the seasonality of the flooded areas was not taken into account.

OCE includes the direct oceanic emissions of COS and the indirect oceanic emissions of COS through the oxidation of CS_2 in the atmosphere. The atmospheric oxidation pathway producing COS from CS_2 is relatively well known and occurs on timescales of 1–7 days (Chin & Davis, 1993; Ma et al., 2021). The CS_2 emitted from the ocean is assumed to be instantaneously converted into COS with a well-constrained molar conversion ratio of 0.81 (Chin & Davis, 1993). The direct oceanic emissions of COS and the oceanic emissions of CS_2 have been computed using box models calibrated with ship-borne measurements made in different parts of the globe (Lennartz et al., 2017, 2021).

The indirect oceanic emissions of COS through DMS, OCE_DMS_PISCES, and OCE_DMS, are based on two different approaches. OCE_DMS is a monthly climatology produced from extrapolations of measurements in sea waters distributed unevenly around the globe (Lana et al., 2011). OCE_DMS_PISCES is simulated by the mechanistic model of DMS production of Belviso et al. (2012) coupled to the ocean general circulation and biochemistry model NEMO-PISCES (Nucleus for European Modeling of the Ocean, Pelagic Interaction Scheme for Carbon and Ecosystem Studies). This DMS module includes the influence of nutrient dynamics (specifically phosphorus limitation) on the concentrations of DMS in sea waters, enabling a better account for the most oligotrophic

subtropical zones of the global ocean. Compared to the Lana et al. (2011) climatology, the coupling between a DMS module and an ocean general circulation model allows consideration of the effects of the horizontal and vertical transport of water masses on the DMS concentrations, which can be important at high latitudes. Recently, the climatology of Lana et al. (2011) has been updated using additional sea water measurements and a refined extrapolation method (Hulswar et al., 2022). The spatial distribution of the new DMS fluxes is now closer to the mechanistic representation of these fluxes from Belviso et al. (2012), with larger summer emissions in the southern high latitudes. The DMS emitted by the oceans is assumed to be instantaneously oxidized into COS in the atmosphere using a reaction rate of 0.7% (Barnes et al., 1994), as suggested by the International Union of Pure and Applied Chemistry (IUPAC; Atkinson et al., 2004). However, the conversion factor is much more uncertain than for CS_2 since the chamber studies were carried out in unrealistic atmospheric conditions, with high DMS concentrations and low NOx conditions (Barnes et al., 1994). The recent identification of novel DMS oxidation products (Jernigan et al., 2022) revises our understanding of the mechanistic links between DMS and COS formation in the atmosphere and challenges this hypothesis. This would imply that the emissions of marine DMS and the indirect production of COS through DMS could have different spatial patterns (see Discussion).

The open burning inventory emissions from Stinecipher et al. (2019), available for the period 1997–2016, include emissions from savanna and grassland, boreal forests, temperate forests, tropical deforestation and degradation, peatland fires, and agricultural waste burning. The inventory is scaled from CO emissions using the GFED Global Fire Emissions Database (GFED version 4, https://www.globalfiredata.org/). Biomass burning sources from agricultural residues and biofuels were not included in the absence of a global map although they were shown to be 3 times as large as open burning emissions over northern America (Campbell et al., 2015). In the Supplement, the Stinecipher et al. (2019) inventory is compared with the GFED v4.1 and Community Emissions Data System (CEDS; Hoesly et al., 2018; see Figure S12 in Supporting Information S1), that includes additional biofuel use, with a global total of 118–154 $GgS.yr^{-1}$ over the period 2010–2018 estimated in Ma et al. (2021). Choosing one inventory over the other is not expected to change the findings of this study.

For the anthropogenic fluxes, ANT, we used the inventory elaborated by Zumkehr et al. (2018), which includes, in order of importance, anthropogenic emissions from the rayon (staple and yarn) industry, residential coal production, pigment production, aluminum melting, agricultural chemical production, and vulcanization of rubber in tyre production. The emissions are mainly located over China and Europe. These emissions arise both from direct COS emissions and indirect COS emissions through atmospheric oxidation of CS_2, that is supposed to be instantaneous and to occur at the surface. The sources of CS_2 arise mainly from the rayon industry located in Eastern China, Eastern Asia, and India.

2.3. Measurements and Data Sampling

We evaluated the simulations of COS mixing ratio against measurements between 2012 and 2018 from 15 stations operated by the NOAA Global Monitoring Earth System Research Laboratory (NOAA/GML; Table 1; available at https://gml.noaa.gov/hats/gases/OCS.html, last access: 9 February 2023). The locations of the station are depicted on Figure 1. The COS samples have been collected as paired flasks one to five times a month since 2000 and have been analyzed with gas chromatography and mass spectrometry detection. Only COS measurements with a difference between the paired flasks of less than 6.3 ppt are considered. These data are an extension of the measurements first published in Montzka et al. (2007). In addition, we used the French sampling site, GIF, located about 20 km to the south west of Paris where ground-level COS has been monitored on an hourly basis since August 2014 (Belviso et al., 2022, Table A1). More details of the surface sites can be found in Table A1.

To investigate the impact of transport errors on the vertical distribution of COS, we compared model results to 2010–2011 NOAA airborne data located at 11 sites over North America: TGC (Sinton, Texas: 27.73°N, 96.86°W), CMA (Cape May, New Jersey: 38.83°N, 74.32°W), HIL (Homer, Illinois: 40.07°N, 87.91°W), CAR (Briggsdale, Colorado: 40.37°N, 104.30°W), BNE (Beaver Crossing, Nebraska: 40.80°N, 97.18°W), THD (Trinidad Head, California: 41.05°N, 124.15°W), WBI (West Branch, Iowa: 41.73°N, 91.35°W), NHA (Worcester, Massachusetts: 42.95°N, 70.63°W), LEF (Park Falls, Wisconsin: 45.95°N, 90.27°W), ESP (Estevan Point, British Columbia: 49.58°N, 126.37°W), ETL (East Trout Lake, Saskatchewan: 54.35°N, 104.98°W). These data are from the aircraft program (Sweeney et al., 2015) that was described for COS measurements at a subset of these sites in Montzka et al. (2007). The upper altitude that was typically reached by this sampling program is 8 km. Further details about the sites can be found in Sweeney et al. (2015). Note that, due to the limited amount of

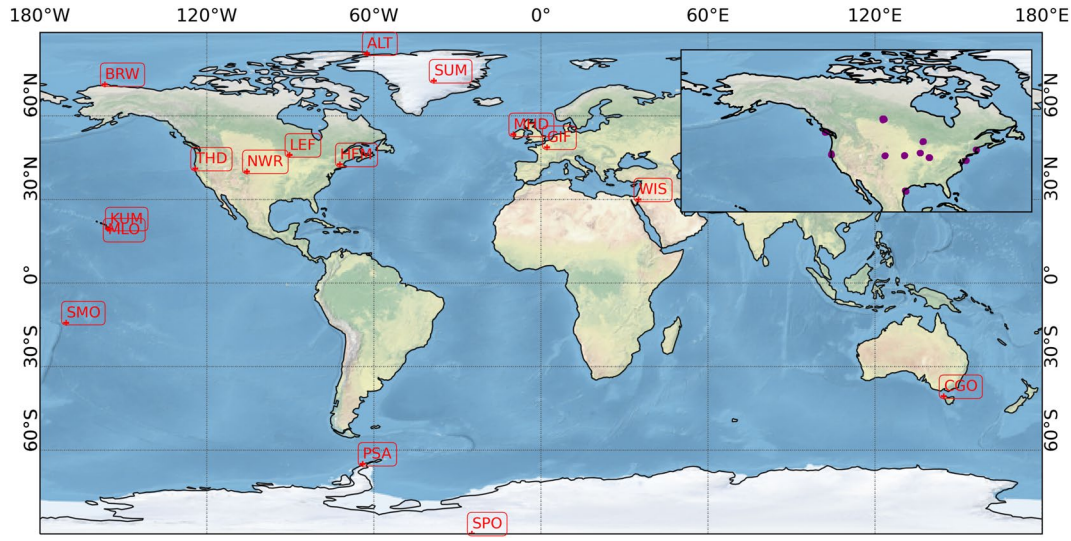

Figure 1. Geographical locations of the NOAA ground-based observations (red stars) and the NOAA profile program (violet filled circles, inset).

airborne data available at that time, we included the spin-up years for this comparison. However, the annual variability of the vertical gradient simulated by the ATMs is small so it should not affect the statistics.

2.4. Emission Scenarios: The Different Experiments

The bottom-up emission scenarios with their associated source and sink components of COS considered in this study are described in Table 3. The control (**Ctl**) scenario represents the state-of-the-art in the COS global budget, as it combines the main known COS fluxes. Only volcano emissions, in the range 23–43 GgS.yr^{-1} (Whelan et al., 2018), and emissions from anoxic soils estimated to about 100 GgS.yr^{-1} (Abadie et al., 2022), have not been considered. Compared to previous studies (see Table 1 of Remaud et al., 2022), the budget for **Ctl** is almost closed with an imbalance of only −37 GgS.yr^{-1} and leads to nearly stable atmospheric mixing ratios at surface sites (see Figure S1 in Supporting Information S1). However, we did not take into account the chemical removal terms in this study: the photolysis loss of COS in the stratosphere amounting to around 50 GgS.yr^{-1} and the oxidation loss of COS in the troposphere amounting to around 100 GgS.yr^{-1} (Whelan et al., 2016). If the chemical removal terms were included, the budget would be negatively unbalanced by 200 GgS.yr^{-1}, which deviates from the −37 GgS.yr^{-1}. The maps of the surface fluxes for scenario **Ctl** are shown on Figures S13 and S14 in Supporting Information S1.

The **Diurnal** scenario differs from the **Ctl** scenario in that it uses biosphere fluxes (soil and vegetation) with a 3-hourly temporal resolution instead of a monthly resolution. Comparing scenarios **Ctl** and **Diurnal** addresses research question 3.

The final two emission scenarios, **Bio2** and **Ocean2**, aim to investigate the influence of a change in terrestrial and oceanic fluxes on atmospheric surface mixing ratios. The **Bio2** scenario differs from the **Ctl** scenario in that the biosphere

Table 3
Description of the Emission Scenarios

Name	Transported fluxes	Source-sink balance	ATMs
Ctl	ANT + BB + OCE + OCE_DMS + BIO_SIB4 (monthly)	−37 GgS.yr^{-1}	All (see Table 1)
Diurnal	ANT + BB + OCE + OCE_DMS + BIO_SIB4_Diurnal	12 GgS.yr^{-1}	LMDz, TM5, TM3, MIROC4, NICAM5, NICAM6
Bio2	ANT + BB + OCE + OCE_DMS + BIO_ORC	−72 GgS.yr^{-1}	LMDz
Ocean2	ANT + BB + OCE + OCE_DMS_PISCES + BIO_ORC	11.7 GgS.yr^{-1}	LMDz

Note. Note that the budget does not include chemical removal terms of ∼150 GgS.yr^{-1} (Whelan et al., 2018). The acronyms of the transported fluxes are described in Table 2.

fluxes are BIO_ORC (simulated by the ORCHIDEE LSM) instead of BIO_SIB4 (simulated by the SIB4 LSM). The **Ocean2** scenario differs from the **Ctl** scenario in that the DMS oceanic fluxes are OCE_DMS_PISCES (simulated by the NEMO-PISCES ocean model) instead of the OCE_DMS (the climatology used in Lennartz et al., 2017).

Emissions from volcanoes and anoxic soils, stratospheric photolysis, and tropospheric oxidation are not included in any of the emission scenarios.

2.5. Post-Processing of the Simulations and Measurements

In Section 3, the features of interest (annual mean, monthly smoothed seasonal cycle) are derived from the surface mixing ratios using the CCGVU curve fitting procedure developed by Thoning et al. (1989) (Carbon Cycle Group Earth System Research Laboratory (CCG/ESRL), NOAA, USA). The CCGVU procedure is fully described and freely available at http://www.esrl.noaa.gov/gmd/ccgg/mbl/crvfit/crvfit.html. The procedure estimates a smooth function by fitting the time series to a first-order polynomial equation for the growth rate combined with a two-harmonic function for the annual cycle and with the residuals that are filtered with a low-pass filter using 80 and 667 days as short-term and long-term cutoff values, respectively. The seasonal cycle and annual gradient are extracted from the smooth function. In addition, outliers are discarded if their values exceed three times the standard deviation of the residual time series.

3. Results

3.1. Impact of Different Transport Models: Using One Flux Scenario

3.1.1. General Behavior: Zonal Mean Structure

We first study the zonal mean structure of the COS simulations. We focus on the boreal summer (June-July-August - JJA) as convection is more active over the continents in the NH, which causes the spread among the models to be the largest. Moreover, the use of COS as a photosynthesis tracer requires quantifying the transport errors during boreal summer, when photosynthesis is more active.

With the **Ctl** scenario, Figure 2 shows that the zonal mean distribution of COS averaged over the transport models exhibits a strong meridional gradient in boreal summer with higher COS values in the NH. The COS source outweighs the terrestrial sink, leading to a net accumulation of COS mole fractions at the surface during winter. The reader is referred to Section 3.2 for a decomposition of the COS total surface mole fractions into the signals caused by the different COS budget components. In addition, Figure 2 depicts the zonal mean distribution of the difference of COS mole fractions between each model and the multi-model average. The model spread of COS mole fractions is the largest below 800 hPa and above 40°N, where surface fluxes are the largest. The spread of COS mole fractions at the surface reflects different strengths of vertical mixing within the tropospheric column. Indeed, a positive anomaly of surface COS mole fractions at the surface compared to the multi-model average is often associated with a negative anomaly in the mid-troposphere. In particular, higher surface mole fractions of COS in the NICAM, MIROC4 and LMDz ATMs suggest that there is, on average, less convection penetrating into the upper troposphere in these models compared to the TM5 and TOMCAT ATMs. The comparison between the NICAM5 and NICAM6 ATMs indicates a modest contribution of the model horizontal resolution to the model spread, as observed by X. Lin et al. (2018). This is also in agreement with Remaud et al. (2018) who showed that the convective and the planetary boundary layer parameterization schemes have larger impact on the CO_2 mole fractions in the low and mid-troposphere relative to the impact of horizontal and vertical resolutions.

In the three models exhibiting less vertical mixing, two of them, the TOMCAT and TM5 ATMs use the convective masses fluxes from the ERA-Interim reanalysis averaged to their lower resolution model grid. The TM3 ATM is based on Tiedtke (1989) which has been recognized to trigger convection too often (Hirons et al., 2013). In the models exhibiting less vertical mixing, the original formulation of the convective schemes has been modified to depart from the convective quasi-equilibrium assumption proposed by Arakawa and Schubert (1974) and to prevent deep convective clouds from developing too often, especially in a too-dry environment. In the LMDz ATM, the original closure based on the CAPE of the Emanuel (1991) scheme was replaced by a closure based on sub-cloud processes that enables deep convection to be delayed later in the afternoon and reduced in intensity (Rio & Hourdin, 2008). The entrainment function in the mixtures has also been modified to be more sensitive to relative humidity of the environment (Grandpeix et al., 2004). In the MIROC4 ATM, a threshold as a function

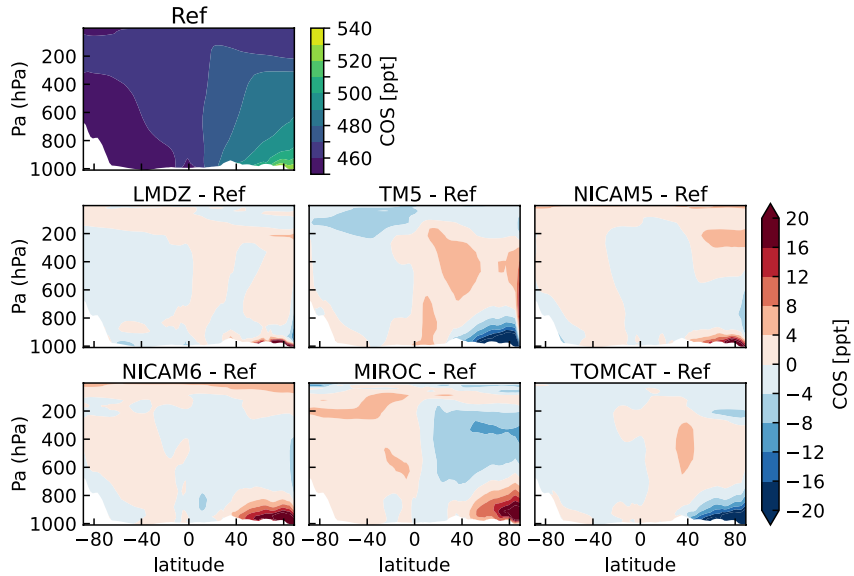

Figure 2. Top row: Zonal mean mole fraction of carbonyl sulfide (COS; ppt) for the reference for the **Ctl** scenario. The reference is the average of COS over all transport models, calculated for the summer months (June, July, August) in 2012–2018. The resulting COS abundances have been shifted by +396 ppt, which brings the reference close to the observed concentrations averaged over all surface sites for January averaged over the years 2012–2018. Second and third rows: Zonal mean mole fraction difference between each individual transport model and the reference.

of relative humidity has been implemented in the Arakawa and Schubert (1974) scheme to prevent convection from triggering when the relative humidity is too low. In the NICAM ATM, the Chikira and Sugiyama (2010) scheme varies the entrainment rate vertically, depending on the humidity and temperature profiles. These implementations generally lead to a more realistic tropical variability (J.-L. Lin et al., 2006) and could explain why the vertical mixing is weaker in MIROC 4, LMDz, and NICAM.

It should be noted that, in agreement with previous studies (Patra et al., 2011; Saito et al., 2013), the meridional gradient of COS reflects the intensity of the IH exchanges and seems to be controlled by the vertical gradient in the NH. Indeed, in the middle troposphere, a negative anomaly of COS mixing ratio in the NH is combined with a positive anomaly of the COS mixing ratio in the SH in most models exhibiting less vertical mixing (MIROC, NICAM 5& 6). In contrast, in models exhibiting stronger vertical mixing, a positive anomaly of COS in the NH is associated with a negative anomaly of COS in the SH. To conclude, the model spread of COS mixing ratio is the largest above 40°N and is mainly determined by the sub-grid scale parameterizations (planetary boundary layer and convective schemes) as they drive the strength of the vertical mixing within the column.

3.1.2. Latitudinal Gradient at Surface Stations

The latitudinal gradient of COS mole fractions reflects the latitudinal surface flux distribution and the intensity of the IH exchange (Denning et al., 1999). Figure 3 shows the observed and simulated mixing ratios at the surface stations as a function of the latitude in February and August. The latitudinal gradient of COS mole fractions in August (February) is representative of the latitudinal gradient in boreal summer (winter; see Figure S4 in Supporting Information S1 for the other months). These 2 months are shown rather than the annual mean (see Figures S3 in Supporting Information S1) as the model spread is season-dependent, being maximum in boreal summer over the continents. It also allows us to disentangle the contributions of the ocean and biosphere fluxes to the IH gradient as they exhibit a strong seasonality (see Figure 7). The simulated COS mixing ratios are averaged over time at each surface station. Since the simulations start from a null initial state, the simulated COS mole fractions have been increased by 500 ppt to match the annual mean COS observations. In February, the distribution of the observed surface mixing ratios is relatively flat over all latitudes. In contrast, all models exhibit a COS mole fraction which is 50 ppt lower in the tropics than elsewhere. This suggests that all the models agree on a missing source or a too-strong biosphere sink over the tropics. Given the oceanic footprint of the tropical sites MLO and SMO, previous top-down studies of Berry et al. (2013), Ma et al. (2021), and Remaud et al. (2022) increased the oceanic source over the tropics to decrease the model-observation mismatch. The ATMs are unable

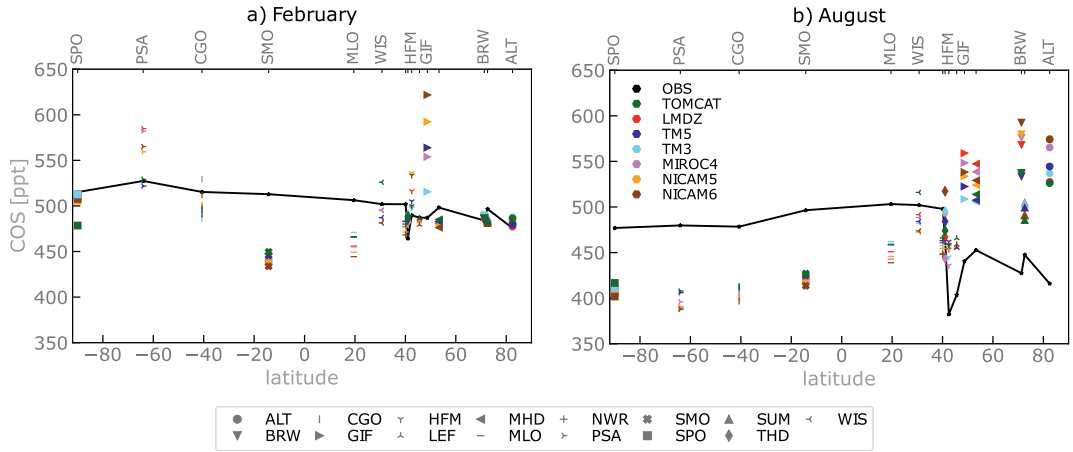

Figure 3. Comparison of the latitudinal variations of the carbonyl sulfide (COS) abundance simulated by several transport models using the **Ctl** surface flux data set (colored dots) with the observations (black line) for February (left), August (right) over the years 2012–2018. The simulated COS abundances have been shifted such that the means are the same as the mean of the observations (~500 ppt). The time series of COS mixing ratio have been detrended and filtered to remove the synoptic variability beforehand. In August, the value at site GIF simulated by the TOMCAT ATM was removed as it was an outlier (value above 800 ppt). For the same reason, the COS values at site GIF simulated by TOMCAT (800 ppt) and LMDz (around 700 ppt) have been removed in February. We removed the site KUM, which is co-located in longitude and latitude with site MLO, for the sake of simplicity. Removing the site KUM does not affect the results.

to represent the negative gradient of 15 ppt from MHD to GIF (see also Figure 11 of Remaud et al., 2022) and instead overestimate the mixing ratio at site GIF by up to 300 ppt. GIF is located in the vicinity of a misplaced hotspot of anthropogenic emissions in the Zumkehr inventory (Belviso et al., 2020; Remaud et al., 2022) while in reality, GIF is comparable to a background station relatively far from major anthropogenic sources (Belviso et al., 2020). Overall, the model spread does not exceed 50 ppt at all sites except at sites PSA and GIF. The spread at PSA arises from a combination of strong oceanic emissions in austral summer and variation in vertical mixing.

At GIF, the ATM resolutions and the sub-grid scale parameterizations are responsible for the model spread. Indeed, the ATMs with the highest vertical resolution, TOMCAT, NICAM 6 simulate mole fractions up to 300 ppt higher than the ATM with the lowest resolution, the TM3 ATM. It is well known that, as the model resolution increases, the simulated mixing ratios become more sensitive to the detailed distribution of sources that are defined with finer resolution. Likewise, the sensitivity to model errors is enhanced near emission hotspots (X. Lin et al., 2018). Errors in horizontal winds or errors in the vertical mixing can have a large impact with emissions from hotspots being near atmospheric stations, possibly creating biases. For instance, errors in horizontal winds can produce peaks which are not present in the observations (Locatelli et al., 2015). Therefore, extra care should be taken when assimilating stations like GIF to optimize the COS surface fluxes in an atmospheric inverse framework (Remaud et al., 2022).

In August, the observed latitudinal distribution of COS was poorly captured by the ATMs. The observations exhibit a negative latitudinal gradient of almost 100 ppt between ALT and SPO. The lowest values of COS are located in the mid and high northern latitudes where the biosphere absorbs a substantial amount of COS from the atmosphere (Kooijmans et al., 2021; Maignan et al., 2021; Vesala et al., 2022). In contrast, all ATMs simulate a positive IH gradient of 150 ppt between the northern and southern mid-latitudes, with the highest values in the northern high latitudes. Overall, the deviation among models is much broader in August than in February, with a model spread exceeding 70 ppt in the northern high latitudes, for instance at BRW. This is due to the different intensities of the vertical mixing within the column (see Figure 1). The model spread does not exceed 15 ppt elsewhere but remains larger than the measurement uncertainty of 6 ppt.

3.1.3. Mean Seasonal Cycle at Surface Stations

The impact of transport variability on the seasonal cycle is illustrated in Figure 4, which shows the mean seasonal cycle of COS given by all ATMs at sites BRW and MLO. The seasonal cycles at more sites are presented on Figure S5 in Supporting Information S1. BRW is a coastal station located on the Arctic tundra adjacent to the Arctic Ocean. Samples are collected at the BRW station predominantly when air is from the north and east, and has passed most recently over the Arctic Ocean. This air also reflects the influence of surface systems further

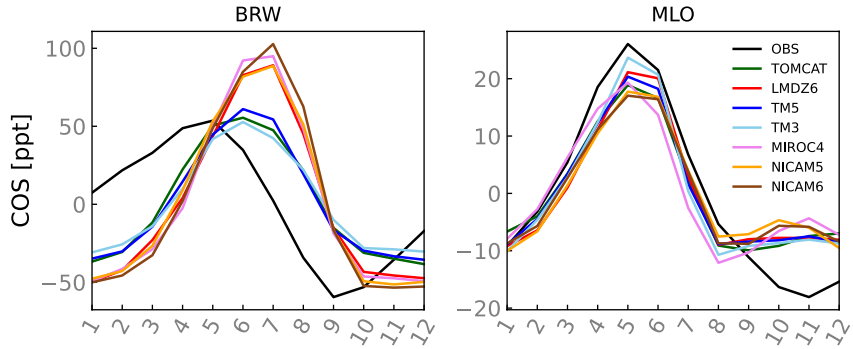

Figure 4. Mean seasonal cycle of the observed (black) and simulated (color) carbonyl sulfide (COS) mixing ratios at sites BRW and MLO averaged over the years 2012–2018. The numbers on the abscissa indicate the months. The curves have been detrended and filtered to remove the synoptic variability.

upwind, such as Siberian forests and mid-latitude regions (Graven et al., 2013; Parazoo et al., 2011). MLO is a high-altitude background station that characterizes the free troposphere in the sub-tropics. Therefore, the seasonal amplitude at site BRW is twice as large as the seasonal cycle amplitude at site MLO. At site BRW, the simulated seasonal cycles lag that of the observations by 1–2 months in all transport models. In the observations, the mole fractions peak in May, whereas the modeled mole fractions peak in July. The reasons of the 1–2 months shift are investigated in Section 3.2 which shows the impact of each flux component on the simulated COS values. Focusing on the model spread, two groups of models can be distinguished: models with a large seasonal amplitude of 150 ppt and a weak vertical mixing (LMDz, NICAM 5&6, MIROC4) and models with a small seasonal amplitude of 90 ppt and a strong vertical mixing (TOMCAT, TM3, TM5). It should be noted that the models with a large seasonal cycle amplitude have a steeper latitudinal gradient in August, as explained by Denning et al. (1995). Compared to the site BRW, the models capture the phase of the seasonal cycle at site MLO relatively well, and their seasonal amplitudes diverge by not more than 20 ppt. However, all models underestimate the seasonal amplitude by 20 ppt and do not represent the observed minimum in November. The seasonal cycles at more sites are presented on Figure S5 in Supporting Information S1.

The performance of the transport models for the seasonal cycle amplitude is statistically evaluated for each surface station in the top panel of Figure 5. The complete mean seasonal cycle for each station and each model is shown on Figure S4 in Supporting Information S1. The models capture the seasonal cycle amplitude well at the low latitude sites SMO, KUM, MLO, WIS, and at site NWR. These sites, representative of background air masses, exhibit a small seasonal amplitude of less than 50 ppt. At the most southern sites (SPO, PSA, CGO), the models overestimate the seasonal amplitude by at least 50 ppt. Since these stations sample air masses mainly coming from the Southern Ocean (Montzka et al., 2007; Remaud et al., 2022), an overestimated amplitude is likely caused by too

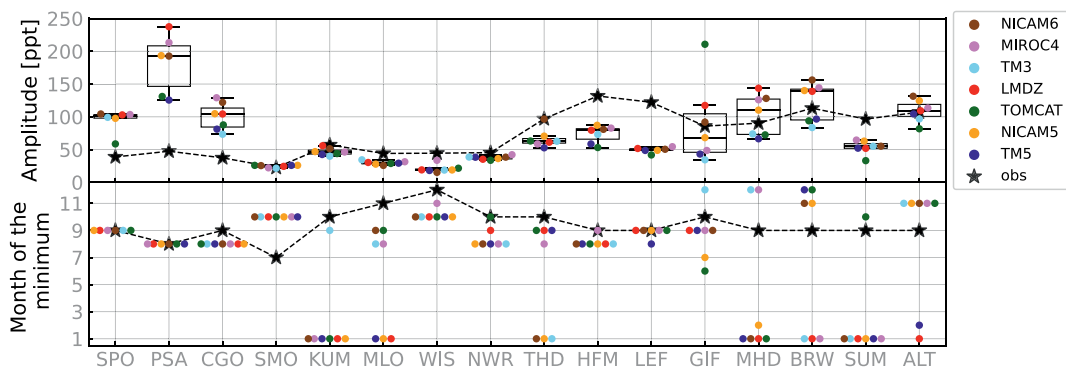

Figure 5. Top: Mean seasonal amplitude (maximum minus minimum mole fraction) of the observed (black stars) and simulated (colored dots) carbonyl sulfide (COS) mole fraction at 15 surface sites. Each colored dot corresponds to the mean seasonal amplitude of COS mixing ratio simulated by a different atmospheric transport model for the **Ctl** scenario. Boxplots of the mean seasonal amplitude of simulated COS mole fractions are superimposed. Bottom: Month of the minimum of the mean seasonal cycle for the observations (black) and for the several transport models (colored dots). For each site, the COS time series have been detrended and filtered to remove the synoptic variability.

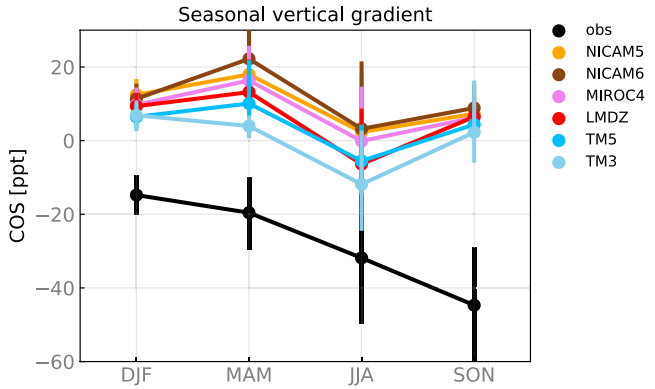

Figure 6. Seasonal mean observed and simulated carbonyl sulfide (COS) gradient between 1 and 4 km (mole fractions at 1 km minus mole fractions at 4 km) averaged over airborne stations located over North America for the **Ctl** scenario. For each subregion, the monthly COS gradients are calculated by averaging the differences in COS concentrations between 1 and 4 km over all the vertical profiles. For each season, the error bar represents the standard deviation of the seasonal COS gradient. DJF: December-January-February, MAM: March-April-May, JJA: June-July-August, SON: September-October-November.

strong oceanic emissions in austral summer. In contrast, the seasonal amplitude is underestimated by 50 ppt at continental sites THD, HFM, and LEF. Since the seasonal amplitude to a great extent reflects the amount of COS absorbed by plants at these sites (Blake et al., 2008; Campbell et al., 2008; Montzka et al., 2007), a too-small simulated seasonal cycle amplitude likely arises from a too weak photosynthesis sink during the growing season. Focusing on the transport errors, the spread is greater than 50 ppt at site PSA, located in the Southern Ocean, and sites MHD, GIF, BRW, ALT. As illustrated in Figure 4, differences in the strength of the vertical mixing within the column mainly contribute to the model spread. Only at station GIF, the resolution is also crucial. It should be noted that the mean mole fractions showed the largest model spread also at these stations. To evaluate the simulated seasonal cycle phase, the bottom panel of Figure 5 focuses on the month of the minimum concentration of the mean seasonal cycle for each site. A striking feature is that, at mid and high latitudes sites MHD, SUM, BRW, ALT, the seasonal minimum occurs in September in the observations. In the models, this minimum occurs between 1 and 3 months later between October and January, as illustrated in Figure 4. At sites LEF, NWR, THD, HFM over North America, the models tend to simulate an earlier minimum crossing of at least 1 month. This might be related to the too weak terrestrial sink.

3.1.4. Mid-Troposphere Seasonal Variations Over North America

The vertical gradient between the boundary layer and the free troposphere reflects the effects of the surface fluxes and the atmospheric transport. Figure 6 shows the seasonal cycle of the vertical gradient of COS between altitudes of 1 and 4 km averaged over the airborne sampling over North America (see Figure 1). Since westerly winds prevail throughout the year in the entire free-troposphere at each site (Sweeney et al., 2015), oceanic air masses from the Pacific Ocean move across the North American continent and mix with air that has been in contact with the biosphere and anthropogenic emissions. Thus, these sites sample both continental and oceanic air masses, with the proportion of oceanic air decreasing from the west to the east of America. The observations show a negative mean vertical gradient throughout the year, decreasing from −18 ppt in DJF (December, January, February) to −40 ppt in SON (September to November). This suggests that, on average, continental North America behaves as a COS sink. The strongest decrease reaches 15 ppt and occurs during the growing season, between MAM and SON. The large depletion of COS within the boundary layer seen in airborne profiles over North

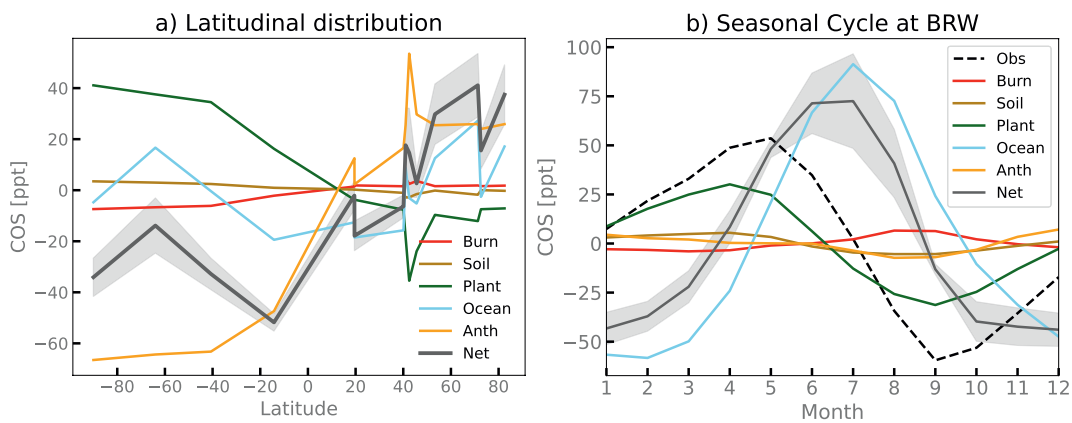

Figure 7. (a) Simulations of the IH gradient of tropospheric carbonyl sulfide (COS) mole fractions at NOAA surface stations. The net signal (gray line) is obtained from a multi-model average of global simulations using the **Ctl** emissions, while the colored lines are obtained by running the global atmospheric simulations with one component flux at a time. The shaded area represents the model spread. (b) Simulations of the seasonal cycle of tropospheric COS mixing ratios at the Barrow Atmospheric Baseline Observatory (BRW) averaged over all transport models. The shaded area is the standard deviation around the mean COS seasonal cycle associated with the different transport models. The dotted black line represents the observed seasonal cycle. Each curve has been detrended and filtered to remove the synoptic variability.

America has been reported previously to be concomitant to depletion of CO_2, indicating a strong and common biosphere sink during this season (Blake et al., 2008; Campbell et al., 2008; Parazoo et al., 2021).

In contrast to the observations, all ATMs show a mean positive vertical gradient all year round, except during JJA when gradients simulated by LMDz, TM3, and TM5 become slightly negative. The model spread is less than 10 ppt and reaches 15 ppt in JJA, much smaller than the mean bias of at least 30 ppt. The model spread and the observed and simulated standard deviation are higher in MAM and JJA. In summer, the weakening of the winds over the middle of the continent and over the east coast leads to less homogeneous vertical profiles in the free troposphere (Sweeney et al., 2015). Combined with enhanced convection, this effect might reinforce the model spread and the simulated standard deviation. Considering the model spread, the models underestimate the sharp decrease of vertical gradient in MAM by 50% and do not prolong this decrease in SON. This model-observation mismatch is consistent with an underestimation of the mean seasonal cycle amplitude at sites HFM, LEF, THD. Kooijmans et al. (2021) showed that, on average, the SIB4 LSM using the Berry et al. (2013) model for the plant uptake, combined to the Ogee et al. (2016) soil model with variable COS mole fractions, underestimates the COS terrestrial sink (soil and plant uptake) during the growing season over FLUXNET sites located in Europe and North America. Parazoo et al. (2021) came to the same conclusion by evaluating the SIB4 plant uptake against airborne measurements over three diverse regions in North America: the crop-dominated Midwest, evergreen-dominated south, and deciduous broadleaf-dominated northeast. The model deficiency can arise from unconstrained parameters specific to the soil and vegetation models representing the COS biosphere exchanges (see Section 3.2 from Kooijmans et al., 2021; Abadie et al., 2022), from missing processes but also from a poor representation of other processes such as photosynthesis that drives the COS biosphere exchanges. In particular, Parazoo et al. (2021) showed that, in southern evergreen forests in North America, the photosynthetic carbon uptake was too weak in late summer in the SIB4 LSM, which is consistent here with an underestimated COS depletion in SON in Figure 5.

3.2. Impact of Each Flux Components on COS Surface Mole Fractions

In order to interpret the model-observation comparison of Figure 3, Figure 7a presents the contributions of the COS budget components to the simulated IH gradient. Results represent the average over all ATMs participating in this intercomparison experiment. The strongly positive latitudinal gradient is driven by the anthropogenic component and to a lesser extent by the ocean emissions. The oceanic component is characterized by two-mole fraction peaks in the southern and northern high latitudes and a minimum mole fraction in the tropics. The positive mole fractions at high latitudes result from the direct oceanic emissions in summer (Lennartz et al., 2017) and the indirect emissions through DMS and CS_2 peaking in the tropics (Lennartz et al., 2020, see also Figure 2 of Remaud et al., 2022). On an annual basis, the plant uptake is characterized by a larger sink in the NH than in the SH. The resulting latitudinal gradient is, however, not sufficient to compensate for the opposing gradients from the ocean and anthropogenic emissions, leading to the overall mismatch observed in Figure 3. The soil and the biomass burning components have a relatively flat distribution and therefore play a minor role in the latitudinal COS gradients.

Figure 7b shows the contributions of the COS budget components - oxic soils, ocean, plant uptake, anthropogenic emissions, biomass burning - to the detrended mean seasonal cycle at site BRW (see Figure S7 in Supporting Information S1 for other sites). The seasonality given by all ATMs is governed by the oceanic and plant uptake components. Since the anthropogenic fluxes do not vary throughout the year, the anthropogenic component of the simulated COS net concentrations is constant all year round, as expected. The weak seasonality of the soil component arises from the COS soil emissions in warmer conditions in summer that offsets the soil uptake in the Ogee et al. (2016) model that is implemented in the SIB4 model (See Figure 3 from Kooijmans et al., 2021). The one to 2 months lag between the observed and simulated concentrations at BRW (see Figure 4) is thus likely induced by too strong oceanic direct emissions at high latitudes in summer or/and an underestimated plant sink in the boreal ecosystems of the NH. An enhanced plant uptake or/and reduced oceanic emissions in the summer high latitudes will also decrease the model observation-mismatch for the IH-gradient (Figure 3). Using an atmospheric inverse framework, Remaud et al. (2022) found that an enhanced COS sink over the boreal regions associated with reduced oceanic summer emission in the Atlantic enables the simulated COS mole fractions to be in better agreement with the airborne measurements from the HIPPO campaign over the Pacific. From a bottom-up modeling perspective, there are some indications that the direct oceanic COS emissions could be overestimated and that the plant uptake is too low in boreal latitudes. For instance, the COS mole fractions given by the ocean box model are higher than most of the measurements made in sea waters sampled over different parts of the globe

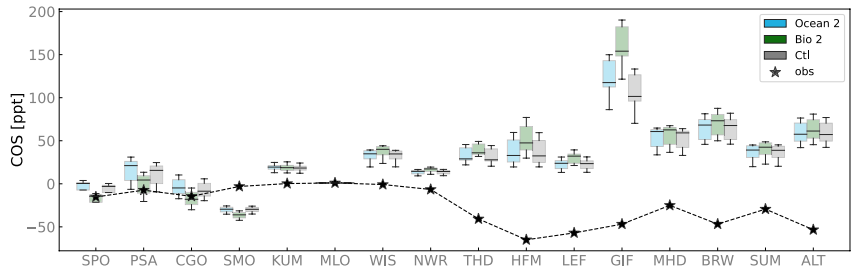

Figure 8. Box-plots of the **annual** simulated mole fraction gradient of carbonyl sulfide (COS) between MLO and the other surface stations for the Ctl (gray), Bio2 (green), Ocean2 (blue) scenarios over the years 2012–2018.

(Lennartz et al., 2017). In addition, Vesala et al. (2022) showed that the biosphere sink in LSMs was too small at a forested boreal site, Hyytiälä, in Finland. Scaled to all evergreen needleleaf forests over the whole boreal region, their empirical model calibrated on observations at Hyytiälä produces a biosphere COS sink that is consistent with the missing COS sink at high northern latitudes in summer identified by our analysis.

3.3. Impact of Different Flux Scenarios on COS Surface Concentrations: Using the Mean Across Transport Models

3.3.1. Changing Model Fluxes

In this part, we assessed the sensitivity of the seasonal cycle and latitudinal distribution to a change in biosphere fluxes and indirect COS emissions through DMS oxidation. For the biosphere part, we consider two sets of biosphere fluxes produced by the ORCHIDEE LSM (**Bio 2** scenario) and the SIB4 LSM (**Ctl** scenario). Compared to the SIB4 LSM, land uptake in the ORCHIDEE LSM is 40% lower over the tropical forests and over the eastern North America (see Figure S8 in Supporting Information S1). To assess the sensitivity of the COS surface mole fractions to a change in the ocean component, we compare the **Ctl** scenario against the **Ocean 2** scenario. The differences between the two fluxes are noticeable mainly over the subtropical oligotrophic gyres and over southern high-latitude oceans where the Belviso et al. (2012) DMS fluxes are 80% higher (see Figure S9 in Supporting Information S1). In contrast, the latter are 50% weaker over the Western Pacific, which is not in line with the missing source location inferred by top-down studies (Glatthor et al., 2015; Kuai et al., 2015; Remaud et al., 2022). The updated version of the Lana et al. (2011) DMS climatology shows less DMS emissions over the Western Pacific and over the Southern Indian Ocean (Hulswar et al., 2022). The reader is referred to Section 2.2 for a description of these oceanic and biosphere fluxes.

The annual gradient between a station and the MLO reference station relates to transport of source/sinks within the regional footprint area of the station as well as to the background gradient caused by remote sources and their transports. Figure 8 shows the boxplots of the mean annual gradients to MLO for all stations for the observations and all ATMs. As the stations are ranked according to their latitudes, Figure 8 enables us to compare the annual latitudinal repartition of COS simulated by all ATMs using three scenarios, **Ocean 2**, **Bio 2**, and **Ctl**. Except at site GIF, the change in either biosphere fluxes or oceanic fluxes is translated into a change in mixing ratio that is smaller than 10 ppt and also smaller than the model spread. The latter exceeds 50 ppt at northern latitudes. At sites GIF, HFM, LEF, the annual gradient to MLO is more sensitive to the biosphere fluxes as the site is mainly influenced by continental air masses.

Figure 9 compares the mean seasonal cycle in terms of amplitude (top panel) and phase (bottom panel) simulated by all ATMs using three scenarios, **Ocean 2**, **Bio 2**, and **Ctl**. On the amplitude, the effects of the biosphere and DMS fluxes are negligible compared to the model spread at most sites. The seasonal amplitudes at sites HFM and LEF are more sensitive to the biosphere fluxes than to the transport model and to the DMS fluxes as these sites sample continental air masses coming primarily from areas covered by vegetation. The site HFM is located in a forest that, on average, absorbs COS over the year (Commane et al., 2015). It should be noted that at sites HFM and LEF, the ORCHIDEE LSM simulates smaller seasonal cycle amplitudes than the SIB4 LSM. This is first because the ORCHIDEE LSM has a smaller plant absorption of COS than the SIB4 LSM over North America, also reflected by the global plant sink of COS (see Figure S8 in Supporting Information S1) of −514 GgS.yr^{-1} (ORCHIDEE) versus −669 GgS.yr^{-1} (SiB4). Second, at site HFM (Harvard Forest), the soil fluxes of Abadie et al. (2022) have a smaller seasonal amplitude (Figure 2 of Abadie et al., 2022) than the soil fluxes from Kooijmans et al. (2021) (Figure 3 of Kooijmans et al., 2021). The absence of seasonal cycle in Abadie

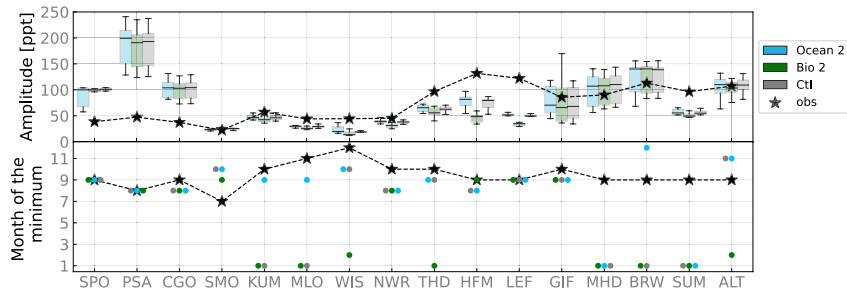

Figure 9. Top: Box-plots of the peak-to-peak amplitude (maximum minus minimum mole fraction) of the mean carbonyl sulfide (COS) seasonal cycle for the **Ctl** (gray), **Bio2** (green), **Ocean2** (blue) scenarios over the years 2012–2018. The black stars correspond to the mean seasonal amplitude for the observed COS mole fractions. The sites are listed on the abscissa. Bottom: Mean time of minimum crossing for modeled (colored dots) and observed (black stars) COS for each scenario. For each site, the COS time series have been detrended and filtered to remove the synoptic variability.

et al. (2022) is supported by the observations of soil fluxes at Harvard Forest. The too-low seasonal cycle amplitude compared to the observations suggests again an underestimation of the COS plant uptake. Regarding the seasonal cycle phase on the bottom panel of Figure 9, the change in biospheric and oceanic fluxes has a minor effect (by 1 month) on the minimum crossing. Only the seasonal phases at sites KUM and MLO are affected by several months by the change of DMS fluxes as these two stations are located in the Pacific Ocean. Note, however, that SIB4 and ORCHIDEE are the only LSMs to simulate the biosphere COS exchange. If all LSMs could simulate biosphere COS exchanges, the model spread in seasonal amplitude and in latitudinal distribution would be certainly much higher given the current diversity of photosynthetic fluxes simulated by the LSMs (Annav et al., 2013). Note also that the two ocean fluxes only differ by the indirect oceanic emissions of COS through DMS (and not by the direct ocean emissions).

3.3.2. Quantifying the Diurnal Rectifier Effect on Monthly Mean COS Concentrations

The simulated COS diurnal variation reflects the day-night contrast in both the prescribed fluxes and the PBL (planetary boundary layer) vertical mixing. The diurnal variability comes here from the plant fluxes, with minor contribution from the soil fluxes. Plants absorb more COS during the daytime when the stomatal opening enables the photosynthesis to happen. At night, plants continue to absorb COS as the carbonic anhydrase activity does not depend on light intensity (Goldan et al., 1988; Protoschill-Krebs et al., 1996) and the stomatal closure is incomplete. Observed nighttime uptake was shown to be on average 25% of the daytime uptake across several sites located in Western Europe and North America between May and September (Kooijmans et al., 2021). Another part of the diurnal variability is contributed by boundary layer processes: during nighttime, COS accumulates near the surface within the shallower stable boundary layer, whereas during daytime, the low COS concentration caused by the plant uptake is distributed over a deeper convective PBL. Thus, the daily mean COS mixing ratio is expected to be greater than in the absence of boundary layer processes and diurnal plant variability (Denning et al., 1995, 1999). This effect of the diurnal variability on longer time scales is called the diurnal rectifier effect.

Here, we quantify the diurnal rectifier effect on the seasonal variability of COS surface mixing ratios. To this end, Figure 10 shows the difference of monthly mean COS mixing ratio between the **Ctl** scenario and the **Diurnal** scenario for the year 2015 at 16 surface stations. In the **Ctl** scenario, the soil and plant fluxes are prescribed to the ATMs at monthly resolution whereas in the **Diurnal** scenario, the soil and plant fluxes are prescribed at a three-hourly resolution. Averaged over all ATMs, this effect is negligible and is less than the measurement uncertainties of 6 ppt at 11 stations out of 16. Even if the diurnal rectifier effect is more noticeable at sites HFM, LEF, BRW, the difference between the **Diurnal** and **Ctl** scenario does not exceed 20 ppt. In summer, the mainly positive difference in COS surface mixing ratios is induced by the temporal covariance between strong vertical mixing and stronger COS uptake during the day. The difference of monthly mean COS mixing ratio between the **Diurnal** scenario and the **Ctl** scenario results from the plant absorption and not the soil fluxes (see Figure S10 in Supporting Information S1). The soil fluxes have a small diurnal variability, although on average the soil flux becomes slightly less negative during the day when the abiotic production term increases with growing temperature (Abadie et al., 2022). The use of the biosphere fluxes from the ORCHIDEE LSM instead of the SIB 4 LSM leads to the same conclusion (see Figure S11 in Supporting Information S1).

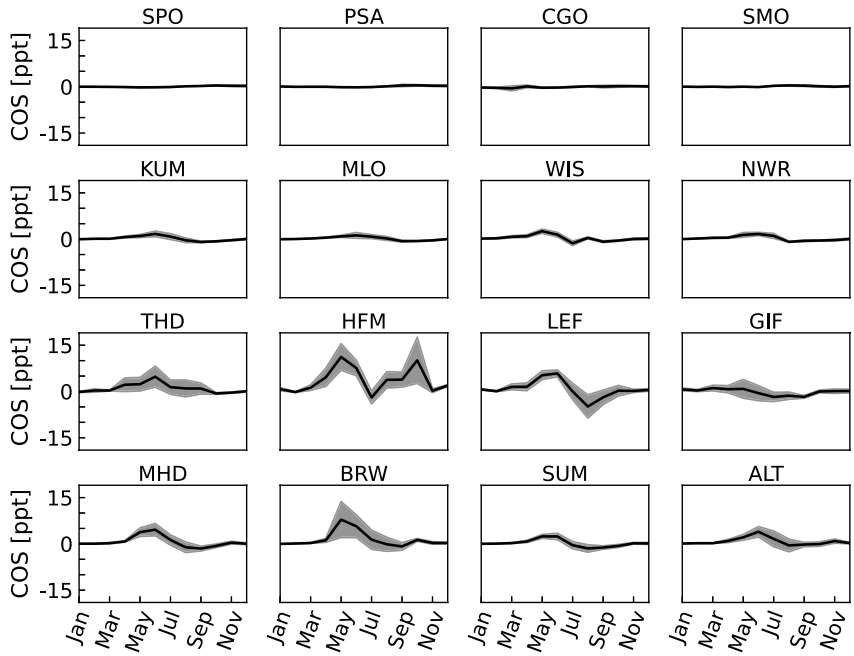

Figure 10. Monthly mean carbonyl sulfide (COS) mole fractions obtained with the **Diurnal** scenario minus monthly mean COS mole fractions obtained with the **Ctl** scenario at each surface station for the year 2015. At each site, the solid line is the mean COS mole fraction across all models, and the shaded envelope represents the standard deviation around the mean.

To conclude, the diurnal rectifier effect for COS can be probably neglected when performing forward and inverse modeling studies to study or assimilate monthly concentrations. This conclusion must be qualified considering the fact that the plant uptake is underestimated in the two LSMs (Kooijmans et al., 2021; Maignan et al., 2021) and that the long-term rectifier effect was not completely assessed. Because of the storage cost of saving 3 hourly fluxes, we only performed 1 yr of the **Diurnal** scenario. Multi-year simulations would allow an assessment of the effect of the rectifier effect on the mean latitudinal gradient (Denning et al., 1995).

4. Summary and Conclusions

With the participation of seven transport models, a control case has been constructed to evaluate the state-of-the-art seasonal fluxes of COS while quantifying the transport errors, as another step to better constrain the COS global budget. We analyzed the concentrations of COS simulated by the ATMs at the location and time of surface and airborne campaign measurements. Specifically, we focused the analysis both on the model-to-model and the model-observations differences in.

1. Large-scale IH gradient, by comparing modeled and observed IH gradients of COS.
2. Simulated seasonal cycles, by comparing with observed seasonal cycles at surface stations.
3. Vertical profiles of COS, by comparing modeled and observed vertical gradients of COS between the PBL and the free troposphere.

In addition, we quantified the sensitivity of the seasonal cycle and the latitudinal distribution of COS to a change in biosphere fluxes and to a change in oceanic fluxes. The diurnal rectifier effect has also been quantified on the seasonal cycle of COS by comparing the monthly mean COS mixing ratios given by three-hourly fluxes and the monthly mean COS mixing ratios given by monthly fluxes for the year 2015.

The main conclusions can be summarized as follows:

1. Overall, the difference between the modeled and observed COS values is larger than the model spread when using state-of-the-art component fluxes.
2. The model spread in COS surface mixing ratios is the largest in summer at northern high latitudes. The model spread at Arctic sites can reach 70 ppt in summer, leading to divergence in seasonal amplitude of more than

50 ppt. Transport errors can potentially lead to significant uncertainties in the northern biosphere sink inferred through atmospheric inverse modeling using COS observations.

3. Concerning the mean seasonal cycle and the latitudinal distribution of COS mole fractions, the model spread in COS simulations is mainly caused by the subgrid-scale parameterizations (convective and boundary layer processes). However, in the vicinity of flux hot-spots, the model resolution becomes crucial.
4. In agreement with earlier studies, model-observation comparisons emphasize the need for a missing tropical source, more biosphere uptake and likely smaller ocean emissions in the NH summer, especially at high latitudes.
5. Based on airborne measurements over North America, models predict a positive vertical gradient between 1 and 4 km, while observations point to a negative gradient all year around, with a stronger gradient in late summer. This again points to the need for stronger COS uptake over North America in the models.
6. Alternative flux combinations lead to similar conclusions. Indeed, the replacement of the biosphere flux simulated by the SIB4 LSM (Kooijmans et al., 2021) by the biosphere fluxes simulated by the ORCHIDEE LSM (Abadie et al., 2022; Maignan et al., 2021) in the **Ctl** scenario leads to minor change in mean seasonal cycle and IH gradient. Likewise, the replacement of the indirect ocean flux through DMS of Lana et al. (2011) by the ocean fluxes from Belviso et al. (2012) in the **Ctl** scenario has a minor impact under the assumption of a global constant conversion factor between DMS and COS (see Discussion below).
7. The diurnal rectifier effect on the mean seasonal cycle is negligible at most surface stations except at a few continental stations over North America where the diurnal rectifier effect does not exceed 30 ppt. This implies that the use of monthly biosphere fluxes instead of three-hourly biosphere fluxes is an acceptable simplification for COS budget studies. However, an assessment of the diurnal rectifier effect on the latitudinal distribution would require the same experiment to be performed but over several years. It would also require improved biosphere fluxes as the current biosphere fluxes are underestimated (Kooijmans et al., 2021).

5. Discussion and Future Work

The atmospheric chemistry of COS was not included in the ATMs used here in order to isolate the transport errors. However, the chemistry related to COS remains poorly resolved. The current understanding of the atmospheric chemistry of COS is that 100 GgS.yr^{-1} is oxidized in the atmosphere and 50 GgS.yr^{-1} is photolyzed in the stratosphere. Because of the small importance of these sinks in the COS budget, their introduction in the ATMs is not expected to modify the conclusions of this study. A second assumption of this study is that the DMS emitted by the ocean is instantaneously oxidized into COS with a yield from Barnes et al. (1994). Recently, a stable intermediate from DMS oxidation, the hydroperoxymethyl thioformate (HPMTF), has been discovered to be the main precursor of COS (Jernigan et al., 2022). The introduction of this chemical pathway in an Atmospheric Chemistry Transport Model led to more COS emissions in the tropics but with a magnitude three times lower than the DMS fluxes used in this study (Jernigan et al., 2022). However, these results are still preliminary. If these reactions are confirmed by more chamber studies and observations in the future, the full chemistry of DMS and COS needs to be taken into account to accurately evaluate the state of the art COS fluxes.

The analysis presented here, focused on the mean seasonal cycle and the IH gradient, could be extended in the future to the interannual variations and the long-term trend of the COS mixing ratios. The trend was not analyzed because some interannual fluxes (e.g., anthropogenic) were not always available. Moreover, the COS mixing ratios derived from the atmospheric inversion of Ma et al. (2021) that was used to rescale the biosphere fluxes were climatological, which is not realistic in regards to the current decreasing trend of COS mole fraction since 2014 and its implication on biosphere fluxes (Belviso et al., 2022).

Finally, the sparse and uneven coverage of the observations limits the evaluation of the COS fluxes to the footprint area of these stations. A complementary paper will also evaluate the COS fluxes using airborne measurements from the NASA Atmospheric Tomography (ATom) Mission (Thompson et al., 2022) and HIAPER Pole-toPole Observations (HIPPO; Wofsy, 2011) campaigns. Although they are limited in time, these measurements will give additional insight to the COS fluxes over the tropical Atlantic and Pacific Ocean. Satellites offer the perspective of constraining the tropical areas over long periods of time (Glatthor et al., 2015; Stinecipher et al., 2022; Vincent & Dudhia, 2017), but the retrievals still entail large uncertainties (Serio et al., 2021; Whelan et al., 2018).

Appendix A: Additional Transport Model Description

A1. LMDz

The LMDz ATM has a spatial resolution of 3.75° × 1.9° (longitude times latitude) with 39 layers in the vertical, based on the general circulation model developed at the Laboratoire de Météorologie Dynamique, LMDz (Hourdin et al., 2020). LMDz6A is our reference version: it was prepared for the 6th Climate Intercomparison Project (CMIP6) as part of the Institut Pierre-Simon Laplace Earth system model. We use the offline version of the LMDz code, which was created by Hourdin and Armengaud (1999) and adapted by Chevallier et al. (2005) for atmospheric inversion. It is driven by air mass fluxes calculated by the complete general circulation model, run at the same resolution and nudged here toward winds from the fifth generation of meteorological analyses of the European Center for Medium-Range Weather Forecasts (ECMWF; ERA5). The off-line model only solves the mass balance equation for tracers, which significantly reduces the computation time. This LMDz version recently participated in the TRANSCOM experiment for CO_2 weather (Zhang et al., 2022).

A2. TM5

TM5 is the global chemistry Transport Model, version 5 (TM5; Krol et al., 2005). It allows two-way nested zooming and is specifically useful for multiple-resolution zooming modeling of trace gases in troposphere and stratosphere. The earlier version of TM5 is the parent TM3 model, which was originally developed by Heimann et al. (1988) and has been widely used in global atmospheric chemistry studies (Friedlingstein et al., 2022; Saunois et al., 2020). TM5 is designed for tracer models and it is used extensively in inversion studies for various trace gases, for example, CO, CO_2, CH_4, and COS. In this study, we used the forward-mode of TM5-4DVAR for COS at a high-resolution of 2° × 2° with vertically 25 layers.

A3. MIROC4

MIROC4-ACTM is a new generation Model for Interdisciplinary Research on Climate (MIROC, version 4.0) based atmospheric chemistry-transport model (Patra et al., 2018). The horizontal triangular truncation at a total horizontal wave number of 42 (T42; latitude and longitude ∼2.81° × 2.81°) is used in the present study. MIROC4-ACTM has a fully resolved stratosphere and mesosphere by implementing the hybrid vertical coordinate of pressure-sigma (surface to about the tropopause) and pressure (about 300 hPa and above). The MIROC4-ACTM has a spectral dynamical core and uses a flux-form semi-Lagrangian scheme for the tracer advection (S.-J. Lin & Rood, 1996). The radiative transfer scheme considers 37 absorption bands, consisting of 23 in the visible and ultraviolet regions enabling better representation of photolysis for chemical species (Sekiguchi & Nakajima, 2008). The cumulus convection scheme is based on Arakawa and Schubert (1974), in which cloud base mass flux is treated as a prognostic variable. The sub-grid vertical mixing is parameterized based on the level 2 scheme of the turbulence closure (Mellor & Yamada, 1982). The model participated in various model intercomparison projects, for example, TransCom-air of air (Krol et al., 2018), and flux inversions are performed for CO_2, CH_4, and N_2O (Chandra et al., 2022; Patra et al., 2022) which have contributed to various international emission and removal budget assessments.

A4. TOMCAT

TOMCAT/SLIMCAT is a global 3-D off-line chemical transport model (Chipperfield, 2006). It is used to study a range of chemistry-aerosol-transport issues in the troposphere and stratosphere. The model is usually forced by ECMWF meteorological (re)analyses, although GCM output can also be used. When using ECMWF fields, as in the experiments described here, the model reads in the 6-hourly fields of temperature, humidity, vorticity, divergence, and surface pressure. The resolved vertical motion is calculated online from the vorticity. Tracer advection is performed using the conservation of second-order moments scheme of Prather (1986). For the experiments described here the model was run at horizontal resolution of 2.8° × 2.8° with 60 hybrid σ-pressure levels from the surface to ∼60 km. The model was forced by ECMWF ERA-Interim reanalyses (Dee et al., 2011). Convective mass fluxes were also taken from ERA-Interim reanalyses and mixing in the boundary layer is based on the scheme of Louis (1979), as described in Stockwell and Chipperfield (1999).

Table A1
List of Air Sampling Sites Selected for Evaluation of Carbonyl Sulfide Concentrations

Site	Short name	Coordinates	Elevation (meters above sea level)	Comments
Gif Sur Yvette, France	GIF	48.42°N–2.08°E	0	
Kennaook/Cape Grim, Australia	CGO	40.68°S, 144.69°E	164	Inlet is 70 m aboveground
Tutuila, American Samoa	SMO	14.25°S, 170.56°W	77	
Mauna Loa, United States	MLO	19.54°N, 155.58°W	3,397	
Cape Kumukahi, United States	KUM	19.74°N, 155.01°W	3	
Niwot Ridge, United States	NWR	40.04°N, 105.54°W	3,475	
Wisconsin, United States	LEF	45.95°N, 90.28°W	868	Inlet is 396 m aboveground on a tall tower
Harvard Forest, United States	HFM	42.54°N, 72.17°W	340	Inlet is 29 m aboveground
Utqiagvik (formerly Barrow), United States	BRW	71.32°N, 155.61°W	8	
Alert, Canada	ALT	82.45°N, 62.51°W	195	
Trinidad Head, United States	THD	41.0°N, 124.1°W		
Mace Head, Ireland	MHD	53.33°N, 9.9°W	18	
Weizmann Institute of Science at theArava Institute, Ketura, Israel	WIS	29.96°N, 35.06°E	151	
Palmer Station, Antarctica (United States)	PSA	64.77°S, 64.05°W	10.0	
South Pole, Antarctica (United States)	SPO	90.0°S, 24.8°E	2,810	
Summit, Greenland	SUM	72.6°N, 38.42°W	3,200	

Note. The sites in orange are coastal. The sites in blue are marine. The sites in brown are continental. The site in black are high-latitude sites.

Data Availability Statement

The source codes of MIROC4-ACTM is described in Patra et al. (2022). The source codes of the TM5 and TM3 models are available at: https://sourceforge.net/projects/tm5/. TM5 is further described in Ma and Krol (2023). The LMDz model is available at http://svn.lmd.jussieu.fr/LMDZ/LMDZ6/ under the CeCILL v2 free software license. The source codes of NICAM-TM are included in the package of the parent model NICAM, which can be obtained upon request under the general terms and conditions (http://nicam.jp/hiki/?Research+Collaborations). TOMCAT/SLIMCAT is a UK community model. It is available to UK (or NERC-funded) researchers who normally access the model on common facilities (e.g., Archer or JASMIN) or who are helped to install it on their local machines. Any potential user interested in the model should contact Martyn Chipperfield. The model updates described in this paper are included in the standard model library. The source codes of the ORCHIDEE version used to produce the terrestrial fluxes are described in Abadie and Maignan (2022). The source codes of the SIB4 version used to produce the terrestrial fluxes are described in Kooijmans et al. (2021). The oceanic emissions of COS and CS2 are available at Lennartz, Gauss, von Hobe, and Marandino (2020). The measurements at site GIF are described in Belviso et al. (2020). All the model outputs (simulated mixing ratios of COS) are available in Remaud et al. (2023).

Acknowledgments
This study was partially funded by the CO_2 Human Emissions (CHE) project, which received funding from the European Union's Horizon 2020 research and innovation programme under Grant 776186. J.M., M.K., and L.K. have been supported by the European Research Council (ERC; Grant 742798). SL acknowledges funding from Grant 16TTP079. P.K.P. and Y.N. are partially supported by the Environmental Research and Technology Development Fund (JPMEERF21S20800) of the Environmental Restoration and Conservation Agency provided by the Ministry of Environment of Japan. YN is also supported by JSPS KAKENHI Grant JP22H05006. M.P.C. and C.W. are supported by the NERC National Centre for Earth Observation CPEO project. The simulations of NICAM-TM were performed by using the supercomputer system of NIES (SX-Aurora TSUBASA). The surface measurements from the NOAA network have been performed by scientists affiliated with NOAA and the Cooperative Institute for Research in the Environmental Sciences (Stephen Montzka, Carolina Siso, Ben Miller, and Isaac Vimont). Dan Yakir facilitates the collection of flask samples at WIS.

References

Abadie, C., & Maignan, F. (2022). Version of ORCHIDEE Land Surface Model used to simulate the COS biosphere fluxes, [Sofware]. Retrieved 1 February 2023 from https://doi.org/10.14768/06dcc7f1-28c2-4ebb-8616-deb0831ffd90

Abadie, C., Maignan, F., Remaud, M., Ogée, J., Campbell, J. E., Whelan, M. E., et al. (2022). Global modeling of soil carbonyl sulfide exchanges. *Biogeosciences*, *19*(9), 2427–2463. https://doi.org/10.5194/bg-19-2427-2022

Anav, A., Friedlingstein, P., Kidston, M., Bopp, L., Ciais, P., Cox, P., et al. (2013). Evaluating the land and ocean components of the global carbon cycle in the CMIP5 Earth system models. *Journal of Climate*, *26*(18), 6801–6843. : https://doi.org/10.1175/JCLI-D-12-00417.1

Arakawa, A., & Schubert, W. H. (1974). Interactions of cumulus cloud ensemble with the large-scale environment, part I. *Journal of the Atmospheric Sciences*, *31*(3), 674–701. https://doi.org/10.1175/1520-0469(1974)031<0674:IOACCE>2.0.CO;2

Atkinson, R., Baulch, D. L., Cox, R. A., Crowley, J. N., Hampson, R. F., Hynes, R. G., et al. (2004). Evaluated kinetic and photochemical data for atmospheric chemistry: Volume I—Gas phase reactions of Ox, HOx, NOx, and SOx species. *Atmospheric Chemistry and Physics*, *4*(6), 1461–1738. https://doi.org/10.5194/acp-4-1461-2004

Barnes, I., Becker, K. H., & Patroescu, I. (1994). The tropospheric oxidation of dimethyl sulfide: A new source of carbonyl sulfide. *Geophysical Research Letters*, *21*(22), 2389–2392. https://doi.org/10.1029/94gl02499

Bechtold, P., Semane, N., Lopez, P., Chaboureau, J.-P., Beljaars, A., & Bormann, N. (2014). Representing equilibrium and nonequilibrium convection in large-scale models. *Journal of the Atmospheric Sciences*, *71*(2), 734–753. https://doi.org/10.1175/JAS-D-13-0163.1

Belviso (2020). Carbonyl sulfide mixing ratios, flux measurements and vertical distribution [Dataset]. Retrieved 1 February 2023 from https://doi.org/10.14768/6800b065-dcec-4006-ada5-b5f62a4bb832

Belviso, S., Lebegue, B., Ramonet, M., Kazan, V., Pison, I., Berchet, A., et al. (2020). A top-down approach of sources and non-photosynthetic sinks of carbonyl sulfide from atmospheric measurements over multiple years in the Paris region (France). *PLoS One*, *15*(2), e0228419. https://doi.org/10.1371/journal.pone.0228419

Belviso, S., Masotti, I., Tagliabue, A., Bopp, L., Brockmann, P., Fichot, C., et al. (2012). DMS dynamics in the most oligotrophic subtropical zones of the global ocean. *Biogeochemistry*, *110*(1–3), 215–241. https://doi.org/10.1007/s10533-011-9648-1

Belviso, S., Remaud, M., Abadie, C., Maignan, F., Ramonet, M., & Peylin, P. (2022). Ongoing decline in the atmospheric COS seasonal cycle amplitude over Western Europe: Implications for surface fluxes. *Atmosphere*, *13*(5), 812. https://doi.org/10.3390/atmos13050812

Berry, J., Wolf, A., Campbell, J. E., Baker, I., Blake, N., Blake, D., et al. (2013). A coupled model of the global cycles of carbonyl sulfide and CO_2: A possible new window on the carbon cycle. *Journal of Geophysical Research: Biogeosciences*, *118*(2), 842–852. https://doi.org/10.1002/jgrg.20068

Blake, N. J., Campbell, J. E., Vay, S. A., Fuelberg, H. E., Huey, L. G., Sachse, G., et al. (2008). Carbonyl sulfide (OCS): Large-scale distributions over North America during INTEX-NA and relationship to CO_2. *Journal of Geophysical Research*, *113*(D9), D09S90. https://doi.org/10.1029/2007JD009163

Campbell, J. E., Carmichael, G. R., Chai, T., Mena-Carrasco, M., Tang, Y., Blake, D. R., et al. (2008). Photosynthetic control of atmospheric carbonyl sulfide during the growing season. *Science*, *322*(5904), 1085–1088. https://doi.org/10.1126/science.1164015

Campbell, J. E., Whelan, M. E., Seibt, U., Smith, S. J., Berry, J. A., & Hilton, T. W. (2015). Atmospheric carbonyl sulfide sources from anthropogenic activity: Implications for carbon cycle constraints. *Geophysical Research Letters*, *42*(8), 3004–3010. https://doi.org/10.1002/2015GL063445

Chandra, N., Patra, P. K., Niwa, Y., Ito, A., Iida, Y., Goto, D., et al. (2022). Estimated regional CO_2 flux and uncertainty based on an ensemble of atmospheric CO_2 inversions. *Atmospheric Chemistry and Physics*, *22*(14), 9215–9243. https://doi.org/10.5194/acp-22-9215-2022

Chevallier, F., Fisher, M., Peylin, P., Serrar, S., Bousquet, P., Breon, F. M., et al. (2005). Inferring CO_2 sources and sinks from satellite observations: Method and application to TOVS data. *Journal of Geophysical Research: Atmospheres, American Geophysical Union*, *110*(D24), D24309. https://doi.org/10.1029/2005JD006390

Chikira, M., & Sugiyama, M. (2010). A cumulus parameterization with state-dependent entrainment rate. Part I: Description and sensitivity to temperature and humidity profiles. *Journal of the Atmospheric Sciences*, *67*(7), 2171–2193. https://doi.org/10.1175/2010JAS3316.1

Chin, M., & Davis, D. D. (1993). Global sources and sinks of OCS and CS2 and their distributions. *Global Biogeochemical Cycles*, *7*(2), 321–337. https://doi.org/10.1029/93gb00568

Chipperfield, M. P. (2006). New version of the TOMCAT/SLIMCAT off-line chemical transport model: Intercomparison of stratospheric tracer experiments. *Quarterly Journal of the Royal Meteorological Society*, *132*(617), 1179–1203. https://doi.org/10.1256/qj.05.51

Commane, R., Meredith, L. K., Baker, I. T., Berry, J. A., Munger, J. W., Montzka, S. A., et al. (2015). Seasonal fluxes of carbonyl sulfide in a midlatitude forest. *Proceedings of the National Academy of Sciences of the United States of America*, *112*(46), 14162–14167. https://doi.org/10.1073/pnas.1504131112

Dee, D. P., Uppala, S. M., Simmons, A. J., Berrisford, P., Poli, P., Kobayashi, S., et al. (2011). The ERA-Interim reanalysis: Configuration and performance of the data assimilation system. *Quarterly Journal of the Royal Meteorological Society*, *137*(656), 553–597. https://doi.org/10.1002/qj.828

Denning, A. S., Fung, I. Y., & Randall, D. (1995). Latitudinal gradient of atmospheric CO_2 due to seasonal exchange with land biota. *Nature*, *376*(6537), 240–243. https://doi.org/10.1038/376240a0

Denning, A. S., Takahashi, T., & Friedlingstein, P. (1999). Can a strong atmospheric CO_2 rectifier effect be reconciled with a "reasonable" carbon budget? *Tellus B: Chemical and Physical Meteorology*, *51*(2), 249–253. https://doi.org/10.3402/tellusb.v51i2.16277

Emanuel, K. A. (1991). A scheme for representing cumulus convection in large-scale models. *Journal of the Atmospheric Sciences*, *48*(21), 2313–2329. https://doi.org/10.1175/1520-0469(1991)048<_x0032_313:ASFRCC>2.0.CO;2

Friedlingstein, P., O'Sullivan, M., Jones, M. W., Andrew, R. M., Gregor, L., Hauck, J., et al. (2022). Global Carbon Budget 2022. *Earth System Science Data*, *14*(11), 4811–4900. https://doi.org/10.5194/essd-14-4811-2022

Glatthor, N., Höpfner, M., Baker, I. T., Berry, J., Campbell, J. E., Kawa, S. R., et al. (2015). Tropical sources and sinks of carbonyl sulfide observed from space. *Geophysical Research Letters*, *42*(22), 10082–10090. https://doi.org/10.1002/2015GL066293

Goldan, P. D., Fall, R., Kuster, W. C., & Fehsenfeld, F. C. (1988). Uptake of COS by growing vegetation: A major tropospheric sink. *Journal of Geophysical Research*, *93*(D11), 14186–14192. https://doi.org/10.1029/JD093iD11p14186

Grandpeix, J.-Y., Phillips, V., & Tailleux, R. (2004). Improved mixing representation in Emanuel's convection scheme. *Quarterly Journal of the Royal Meteorological Society*, *130*(604), 3207–3222. https://doi.org/10.1256/qj.03.144

Graven, H. D., Keeling, R. F., Piper, S. C., Patra, P. K., Stephens, B. B., Wofsy, S. C., et al. (2013). Enhanced seasonal exchange of CO_2 by Northern ecosystems since 1960. *Science*, *341*(6150), 1085–1089. https://doi.org/10.1126/science.1239207

Gurney, K. R., Law, R. M., Denning, A. S., Rayner, P. J., Baker, D., Bousquet, P., et al. (2002). Toward robust regional estimates of CO_2 sources and sinks using atmospheric transport models. *Nature*, *415*(6872), 626–630. https://doi.org/10.1038/415626a

Heimann, M., & Körner, S. (2003). *The global atmospheric tracer model TM3* (p. 5). Technical Reports. Max-Planck-Institut für Biogeochemie

Heimann, M., Monfray, P., & Polian, G. (1988). Long-range transport of ^{222}Rn—A test for 3D tracer models. *Chemical Geology*, *70*(1–2), 98. https://doi.org/10.1016/0009-2541(88)90476-7

Hirons, L. C., Inness, P., Vitart, F., & Bechtold, P. (2013). Understanding advances in the simulation of intraseasonal variability in the ECMWF model. Part II: The application of process-based diagnostics. *Quarterly Journal of the Royal Meteorological Society*, *139*(675), 1427–1444. https://doi.org/10.1002/qj.2059

Hoesly, R. M., Smith, S. J., Feng, L., Klimont, Z., Janssens-Maenhout, G., Pitkanen, T., et al. (2018). Historical (1750–2014) anthropogenic emissions of reactive gases and aerosols from the Community Emissions Data System (CEDS). *Geoscientific Model Development*, *11*(1), 369–408. https://doi.org/10.5194/gmd-11-369-2018

Holtslag, A. A. M., & Moeng, C.-H. (1991). Eddy diffusivity and countergradient transport in the convective atmospheric boundary layer. *Journal of the Atmospheric Sciences*, *48*(14), 1690–1698. https://doi.org/10.1175/1520-0469(1991)048<1690:EDACTI>2.0.CO;2

Hourdin, F., & Armengaud, A. (1999). The use of finite-volume methods for atmospheric advection of trace species, part I: Test of various formulations in a general circulation model. *Monthly Weather Review*, *127*(5), 822–837. https://doi.org/10.1175/1520-0493(1999)127%3C0822:TUOFVM%3E2.0.CO;2

Hourdin, F., Rio, C., Grandpeix, J.-Y., Madeleine, J.-B., Cheruy, F., Rochetin, N., et al. (2020). LMDZ6A: The atmospheric component of the IPSL climate model with improved and better tuned physics. *Journal of Advances in Modeling Earth Systems*, *12*(7), e2019MS001892. https://doi.org/10.1029/2019MS001892

Hu, L., Montzka, S. A., Kaushik, A., Andrews, A. E., Sweeney, C., Miller, J., et al. (2021). COS-derived GPP relationships with temperature and light help explain high-latitude atmospheric CO_2 seasonal cycle amplification. *Proceedings of the National Academy of Sciences of the United States of America*, *118*(33), e2103423118. https://doi.org/10.1073/pnas.2103423118

Hulswar, S., Simó, R., Galí, M., Bell, T. G., Lana, A., Inamdar, S., et al. (2022). Third revision of the global surface seawater dimethyl sulfide climatology (DMS-Rev3). *Earth System Science Data*, *14*(7), 2963–2987. https://doi.org/10.5194/essd-14-2963-2022

Jernigan, C. M., Fite, C. H., Vereecken, L., Berkelhammer, M. B., Rollins, A. W., Rickly, P. S., et al. (2022). Efficient production of carbonyl sulfide in the low-NOx oxidation of dimethyl sulfide. *Geophysical Research Letters*, *49*(3), e2021GL096838. https://doi.org/10.1029/2021GL096838

Kooijmans (2021). Version of the SiB4 Land Surface Model used to simulate the COS exchanges between the atmosphere and the continental surface [Software]. github. Retrieved 1 February 2023 from https://gitlab.com/kdhaynes/sib4_corral

Kooijmans, L. M. J., Cho, A., Ma, J., Kaushik, A., Haynes, K. D., Baker, I., et al. (2021). Evaluation of carbonyl sulfide biosphere exchange in the Simple Biosphere Model (SiB4). *Biogeosciences*, *18*(24), 6547–6565. https://doi.org/10.5194/bg-18-6547-2021

Krol, M., de Bruine, M., Killaars, L., Ouwersloot, H., Pozzer, A., Yin, Y., et al. (2018). Age of air as a diagnostic for transport timescales in global models. *Geoscientific Model Development*, *11*(8), 3109–3130. https://doi.org/10.5194/gmd-11-3109-2018

Krol, M., Houweling, S., Bregman, B., van den Broek, M., Segers, A., van Velthoven, P., et al. (2005). The two-way nested global chemistry-transport zoom model TM5: Algorithm and applications. *Atmospheric Chemistry and Physics*, *5*(2), 417–432. https://doi.org/10.5194/acp-5-417-2005

Kuai, L., Parazoo, N. C., Shi, M., Miller, C. E., Baker, I., Bloom, A. A., et al. (2022). Quantifying northern high latitude Gross Primary Productivity (GPP) using carbonyl sulfide (OCS). *Global Biogeochemical Cycles*, *36*(9), e2021GB007216. https://doi.org/10.1029/2021GB007216

Kuai, L., Worden, J. R., Campbell, J. E., Kulawik, S. S., Li, K.-F., Lee, M., et al. (2015). Estimate of carbonyl sulfide tropical oceanic surface fluxes using Aura Tropospheric Emission Spectrometer observations. *Journal of Geophysical Research: Atmospheres*, *120*(20), 11012–11023. https://doi.org/10.1002/2015JD023493

Lana, A., Bell, T. G., Simó, R., Vallina, S. M., Ballabrera-Poy, J., Kettle, A. J., et al. (2011). An updated climatology of surface dimethlysulfide concentrations and emission fluxes in the global ocean. *Global Biogeochemical Cycles*, *25*(1), GB1004. https://doi.org/10.1029/2010GB003850

Lana, A., Simó, R., Vallina, S. M., & Dachs, J. (2012). Re-examination of global emerging patterns of ocean DMS concentration. *Biogeochemistry*, *110*(1–3), 173–182. https://doi.org/10.1007/s10533-011-9677-9

Launois, T., Peylin, P., Belviso, S., & Poulter, B. (2015). A new model of the global biogeochemical cycle of carbonyl sulfide—Part 2: Use of carbonyl sulfide to constrain Gross Primary Productivity in current vegetation models. *Atmospheric Chemistry and Physics*, *15*(16), 9285–9312. https://doi.org/10.5194/acp-15-9285-2015

Law, R. M., Rayner, P. J., Denning, A. S., Erickson, D., Fung, I. Y., Heimann, M., et al. (1996). Variations in modeled atmospheric transport of carbon dioxide and the consequences for CO_2 inversions. *Global Biogeochemical Cycles*, *10*(4), 783–796. https://doi.org/10.1029/96GB01892

Leer, B. V. (1977). Towards the ultimate conservative difference scheme, IV. A new approach to numerical convection. *Journal of Computational Physics*, *23*(3), 276–299. https://doi.org/10.1016/0021-9991(77)90095-X

Lennartz, S. T., Gauss, M., von Hobe, M., & Marandino, C. A. (2020). Carbonyl sulfide (OCS/COS) and Carbon disulfide (CS2): Global modeled marine surface concentrations and emissions, 2000–2019 (1.0.0) [Dataset]. Zenodo. https://doi.org/10.5281/zenodo.4297010

Lennartz, S. T., Gauss, M., von Hobe, M., & Marandino, C. A. (2021). Monthly resolved modeled oceanic emissions of carbonyl sulfide and carbon disulfide for the period 2000–2019. *Earth System Science Data*, *13*(5), 2095–2110. https://doi.org/10.5194/essd-13-2095-2021

Lennartz, S. T., Marandino, C. A., von Hobe, M., Andreae, M. O., Aranami, K., Atlas, E., et al. (2020). Marine carbonyl sulfide (OCS) and carbon disulfide (CS2): A compilation of measurements in seawater and the marine boundary layer. *Earth System Science Data*, *12*(1), 591–609. https://doi.org/10.5194/essd12-591-2020

Lennartz, S. T., Marandino, C. A., von Hobe, M., Cortes, P., Quack, B., Simo, R., et al. (2017). Direct oceanic emissions unlikely to account for the missing source of atmospheric carbonyl sulfide. *Atmospheric Chemistry and Physics*, *17*(1), 385–402. https://doi.org/10.5194/acp-17-385-2017

Lin, J.-L., Kiladis, G. N., Mapes, B. E., Weickmann, K. M., Sperber, K. R., Lin, W., et al. (2006). Tropical intraseasonal variability in 14 IPCC AR4 climate models. Part I: Convective signals. *Journal of Climate*, *19*(12), 2665–2690. https://doi.org/10.1175/JCLI3735.1

Lin, S.-J., & Rood, R. (1996). Multidimensional flux-form semi-Lagrangian transport schemes. *Monthly Weather Review*, *124*(9), 2046–2070. https://doi.org/10.1175/15200493(1996)124<2046:MFFSLT>2.0.CO;2

Lin, X., Ciais, P., Bousquet, P., Ramonet, M., Yin, Y., Balkanski, Y., et al. (2018). Simulating CH_4 and CO_2 over South and East Asia using the zoomed chemistry transport model LMDz-INCA. *Atmospheric Chemistry and Physics*, *18*(13), 9475–9497. https://doi.org/10.5194/acp-18-9475-2018

Locatelli, R., Bousquet, P., Hourdin, F., Saunois, M., Cozic, A., Couvreux, F., et al. (2015). Atmospheric transport and chemistry of trace gases in LMDz5B: Evaluation and implications for inverse modeling. *Geoscientific Model Development*, *8*(2), 129–150. https://doi.org/10.5194/gmd-8-129-2015

Louis, J.-F. (1979). A parametric model of vertical eddy fluxes in the atmosphere. *Boundary Layer Meteorok*, *17*(2), 187–202. https://doi.org/10.1007/bf00117978

Ma, J., Kooijmans, L. M. J., Cho, A., Montzka, S. A., Glatthor, N., Worden, J. R., et al. (2021). Inverse modeling of carbonyl sulfide: Implementation, evaluation and implications for the global budget. *Atmospheric Chemistry and Physics*, *21*(5), 3507–3529. https://doi.org/10.5194/acp-21-3507-2021

Ma, J., & Krol, M. (2023). COS intercomparison project-TM5 transport model version for COS. [Software]. Zenodo. https://doi.org/10.5281/zenodo.7525670

Maignan, F., Abadie, C., Remaud, M., Kooijmans, L. M. J., Kohonen, K.-M., Commane, R., et al. (2021). Carbonyl sulfide: Comparing a mechanistic representation of the vegetation uptake in a Land Surface Model and the leaf relative uptake approach. *Biogeosciences*, *18*(9), 2917–2955. https://doi.org/10.5194/bg-18-2917-2021

Mellor, G. L., & Yamada, T. (1974). A hierarchy of turbulence closure models for planetary boundary layers. *Journal of the Atmospheric Sciences*, *31*(7), 1791–1806. https://doi.org/10.1175/1520-0469(1974)031<1791:ahotcm>2.0.co;2

Mellor, G. L., & Yamada, T. (1982). Development of a turbulence closure model for geostrophic fluid problems. *Reviews of Geophysics*, *20*(4), 851–875. https://doi.org/10.1029/RG020i004p00851

Meredith, L. K., Boye, K., Youngerman, C., Whelan, M., Ogée, J., Sauze, J., & Wingate, L. (2018). Coupled biological and abiotic mechanisms driving carbonyl sulfide production in soils. *Soil Systems*, *2*(3), 37. https://doi.org/10.3390/soilsystems2030037

Meredith, L. K., Ogée, J., Boye, K., Singer, E., Wingate, L., von Sperber, C., et al. (2019). Soil exchange rates of COS and $CO^{18}O$ differ with the diversity of microbial communities and their carbonic anhydrase enzymes. *The ISME Journal*, *13*(2), 290–300. https://doi.org/10.1038/s41396-018-0270-2

Miura, H. (2007). An upwind-biased conservative advection scheme for spherical hexagonal-pentagonal grids. *Monthly Weather Review*, *135*(12), 4038–4044. https://doi.org/10.1175/2007MWR2101.1

Montzka, S. A., Calvert, P., Hall, B. D., Elkins, J. W., Conway, T. J., Tans, P. P., & Sweeney, C. (2007). On the global distribution, seasonality, and budget of atmospheric carbonyl sulfide (COS) and some similarities to CO_2. *Journal of Geophysical Research*, *112*(D9), D09302. https://doi.org/10.1029/2006JD007665

Nakanishi, M., & Niino, H. (2004). An improved Mellor-Yamada level-3 model with condensation physics: Its design and verification. *Boundary-Layer Meteorology*, *112*, 1–31. https://doi.org/10.1023/B:BOUN.0000020164.04146.98

Niwa, Y., Sawa, Y., Nara, H., Machida, T., Matsueda, H., Umezawa, T., et al. (2021). Estimation of fire-induced carbon emissions from Equatorial Asia in 2015 using in situ aircraft and ship observations. *Atmospheric Chemistry and Physics*, *21*(12), 9455–9473. https://doi.org/10.5194/acp-21-9455-2021

Niwa, Y., Tomita, H., Satoh, M., & Imasu, R. (2011). A three-dimensional icosahedral grid advection scheme preserving monotonicity and consistency with continuity for atmospheric tracer transport. *Journal of the Meteorological Society of Japan*, *89*(3), 255–268. https://doi.org/10.2151/jmsj.2011-306

Niwa, Y., Tomita, H., Satoh, M., Imasu, R., Sawa, Y., Tsuboi, K., et al. (2017). A 4D-Var inversion system based on the icosahedral grid model (NICAM-TM 4D-Var v1.0)—Part 1: Offline forward and adjoint transport models. *Geoscientific Model Development*, *10*(3), 1157–1174. https://doi.org/10.5194/gmd-10-1157-2017

Ogée, J., Sauze, J., Kesselmeier, J., Genty, B., Van Diest, H., Launois, T., & Wingate, L. (2016). A new mechanistic framework to predict OCS fluxes from soils. *Biogeosciences*, *13*(8), 2221–2240. https://doi.org/10.5194/bg-13-2221-2016

Parazoo, N. C., Bowman, K. W., Baier, B. C., Liu, J., Lee, M., Kuai, L., et al. (2021). Covariation of airborne biogenic tracers (CO_2, COS, and CO) supports stronger than expected growing season photosynthetic uptake in the southeastern U.S. *Global Biogeochemical Cycles*, *35*(10), e2021GB006956. https://doi.org/10.1029/2021GB006956

Parazoo, N. C., Denning, A. S., Berry, J. A., Wolf, A., Randall, D. A., Kawa, S. R., et al. (2011). Moist synoptic transport of CO_2 along the mid-latitude storm track. *Geophysical Research Letters*, *38*(9), L09804. https://doi.org/10.1029/2011GL047238

Patra, P. K., Dlugokencky, E., Elkins, J., Dutton, G., Tohjima, Y., Sasakawa, M., et al. (2022). Forward and inverse modeling of atmospheric nitrous oxide using MIROC4-atmospheric chemistry-transport model. *Journal of the Meteorological Society of Japan. Series II*, *100*(2), 361–386. https://doi.org/10.2151/jmsj.2022-018

Patra, P. K., Houweling, S., Krol, M., Bousquet, P., Belikov, D., Bergmann, D., et al. (2011). TransCom model simulations of CH4 and related species: Linking transport, surface flux, and chemical loss with CH4 variability in the troposphere and lower stratosphere. *Atmospheric Chemistry and Physics*, *11*(24), 12813–12837. https://doi.org/10.5194/acp-11-12813-2011

Patra, P. K., Takigawa, M., Watanabe, S., Chandra, N., Ishijima, K., & Yamashita, Y. (2018). Improved chemical tracer simulation by MIROC4.0-based Atmospheric Chemistry-Transport Model (MIROC4-ACTM). *SOLA*, *14*, 91–96. https://doi.org/10.2151/sola.2018-016

Prather, M. (1986). Numerical advection by conservation of second order moments. *Journal of Geophysical Research*, *91*(D6), 6671–6681. https://doi.org/10.1029/JD091iD06p06671

Protoschill-Krebs, G., Wilhelm, C., & Kesselmeier, J. (1996). Consumption of carbonyl sulfide (COS) by higher plant carbonic anhydrase (CA). *Atmospheric Environment*, *30*(18), 3151–3156. https://doi.org/10.1016/1352-2310(96)00026-X

Remaud, M., Chevallier, F., Cozic, A., Lin, X., & Bousquet, P. (2018). On the impact of recent developments of the LMDz atmospheric general circulation model on the simulation of CO_2 transport. *Geoscientific Model Development*, *11*, 4489–4513. https://doi.org/10.5194/gmd-11-4489-2018

Remaud, M., Chevallier, F., Maignan, F., Belviso, S., Berchet, A., Parouffe, A., et al. (2022). Plant Gross Primary Production, plant respiration, and carbonyl sulfide emissions over the globe inferred by atmospheric inverse modeling. *Atmospheric Chemistry and Physics*, *22*(4), 2525–2552. https://doi.org/10.5194/acp-22-2525-2022

Remaud, M., Jin, M., Patra, P., Niwa, Y., Rodenbeck, C., Cartwright, M., & Krol, M. (2023). Intercomparison of atmospheric Carbonyl Sulfide (TransCom-COS; Parts one & two) [Dataset]. Zenodo. https://doi.org/10.5281/zenodo.7632737

Rio, C., & Hourdin, F. (2008). A thermal plume model for the convective boundary layer: Representation of cumulus clouds. *Journal of the Atmospheric Sciences*, *65*(2), 407–425. https://doi.org/10.1175/2007JAS2256.1

Rochetin, N., Grandpeix, J.-Y., Rio, C., & Couvreux, F. (2013). Deep convection triggering by boundary layer thermals. Part II: Stochastic triggering parameterization for the LMDZ GCM. *Journal of the Atmospheric Sciences*, *71*(2), 515–538. https://doi.org/10.1175/JAS-D-12-0337.1

Russell, G. L., & Lerner, J. A. (1981). A new finite-differencing scheme for tracer transport equation. *Journal of Applied Meteorology*, *20*(12), 1483–1498. https://doi.org/10.1175/1520-0450(1981)020<1483:ANFDSF>2.0.CO;2

Saito, R., Patra, P. K., Sweeney, C., Machida, T., Krol, M., Houweling, S., et al. (2013). TransCom model simulations of methane: Comparison of vertical profiles with aircraft measurements. *Journal of Geophysical Research: Atmospheres*, *118*(9), 3891–3904. https://doi.org/10.1002/jgrd.50380

Satoh, M., Tomita, H., Yashiro, H., Miura, H., Kodama, C., Seiki, T., et al. (2014). The non-hydrostatic icosahedral atmospheric model: Description and development. *Progress in Earth and Planetary Science*, *1*, 1–32. https://doi.org/10.1186/s40645-014-0018-1

Saunois, M., Stavert, A. R., Poulter, B., Bousquet, P., Canadell, J. G., Jackson, R. B., et al. (2020). The Global Methane Budget 2000–2017. *Earth System Science Data*, *12*(3), 1561–1623. https://doi.org/10.5194/essd-12-1561-2020

Sekiguchi, M., & Nakajima, T. (2008). A *k*-distribution based radiation code and its computational optimization for an atmospheric general circulation model. *Journal of Quantitative Spectroscopy and Radiative Transfer*, *109*(17–18), 2779–2793. https://doi.org/10.1016/j.jqsrt.2008.07.013

Serio, C., Masiello, G., Mastro, P., Belviso, S., & Remaud, M. (2021). Seasonal variability of degrees of freedom and its effect over time series and spatial patterns of atmospheric gases from satellite: Application to carbonyl sulfide (OCS). *Remote Sensing of Clouds and the Atmosphere XXVI*, *11859*, 11–23. https://doi.org/10.1117/12.2599761

Stinecipher, J. R., Cameron-Smith, P. J., Blake, N. J., Kuai, L., Lejeune, B., Mahieu, E., et al. (2019). Biomass burning unlikely to account for missing source of carbonyl sulfide. *Geophysical Research Letters*, *46*(24), 14912–14920. https://doi.org/10.1029/2019GL085567

Stinecipher, J. R., Cameron-Smith, P. J., Kuai, L., Glatthor, N., Höpfner, M., Baker, I., et al. (2022). Remotely sensed carbonyl sulfide constrains model estimates of Amazon primary productivity. *Geophysical Research Letters*, *49*(9), e2021GL096802. https://doi.org/10.1029/2021GL096802

Stockwell, D. Z., & Chipperfield, M. P. (1999). A tropospheric chemical-transport model: Development and validation of the model transport schemes. *Quarterly Journal of the Royal Meteorological Society*, *125*(557), 1747–1783. https://doi.org/10.1002/qj.49712555714

Suntharalingam, P., Kettle, A. J., Montzka, S. M., & Jacob, D. J. (2008). Global 3-D model analysis of the seasonal cycle of atmospheric carbonyl sulfide: Implications for terrestrial vegetation uptake. *Geophysical Research Letters*, *35*(19), L19801. https://doi.org/10.1029/2008GL034332

Sweeney, C., Karion, A., Wolter, S., Newberger, T., Guenther, D., Higgs, J. A., et al. (2015). Seasonal climatology of CO_2 across North America from aircraft measurements in the NOAA/ESRL global greenhouse gas reference network. *Journal of Geophysical Research: Atmospheres*, *120*(10), 5155–5190. https://doi.org/10.1002/2014JD022591

Thompson, C. R., Wofsy, S. C., Prather, M. J., Newman, P. A., Hanisco, T. F., Ryerson, T. B., et al. (2022). The NASA Atmospheric Tomography (ATom) mission: Imaging the chemistry of the global atmosphere. *Bulletin of the American Meteorological Society*, *103*(3), E761–E790. https://doi.org/10.1175/bams-d-20-0315.1

Thoning, K. W., Tans, P. P., & Komhyr, W. D. (1989). Atmospheric carbon dioxide at Mauna Loa Observatory: 2. Analysis of the NOAA GMCC data, 1974–1985. *Journal of Geophysical Research*, *94*(D6), 8549–8565. https://doi.org/10.1029/JD094iD06p08549

Tiedtke, M. (1989). A comprehensive mass flux scheme for cumulus parameterization in large-scale models. *Monthly Weather Review*, *117*(8), 1779–1800. https://doi.org/10.1175/1520-0493(1989)117<1779:acmfsf>2.0.co;2

Tootchi, A., Jost, A., & Ducharne, A. (2019). Multi-source global wetland maps combining surface water imagery and groundwater constraints. *Earth System Science Data*, *11*(1), 189–220. https://doi.org/10.5194/essd-11-189-2019

Vesala, T., Kohonen, K.-M., Kooijmans, L. M. J., Praplan, A. P., Foltýnová, L., Kolari, P., et al. (2022). Long-term fluxes of carbonyl sulfide and their seasonality and interannual variability in a boreal forest. *Atmospheric Chemistry and Physics*, *22*(4), 2569–2584. https://doi.org/10.5194/acp-22-2569-2022

Vincent, R. A., & Dudhia, A. (2017). Fast retrievals of tropospheric carbonyl sulfide with IASI. *Atmospheric Chemistry and Physics*, *17*(4), 2981–3000. https://doi.org/10.5194/acp-17-2981-2017

Whelan, M. E., Hilton, T. W., Berry, J. A., Berkelhammer, M., Desai, A. R., & Campbell, J. E. (2016). Carbonyl sulfide exchange in soils for better estimates of ecosystem carbon uptake. *Atmospheric Chemistry and Physics*, *16*(6), 3711–3726. https://doi.org/10.5194/acp16-3711-2016

Whelan, M. E., Lennartz, S. T., Gimeno, T. E., Wehr, R., Wohlfahrt, G., Wang, Y., et al. (2018). Reviews and syntheses: Carbonyl sulfide as a multi-scale tracer for carbon and water cycles. *Biogeosciences*, *15*(12), 3625–3657. https://doi.org/10.5194/bg-15-3625-2018

Wofsy, S. C. (2011). HIAPER Pole-to-Pole Observations (HIPPO): Finegrained, global-scale measurements of climatically important atmospheric gases and aerosols. *Philosophical Transactions of the Royal Society A*, *369*(1943), 2073–2086. https://doi.org/10.1098/rsta.2010.0313

Wohlfahrt, G., Brilli, F., Hortnagl, L., Xu, X., Bingemer, H., Hansel, A., & Loreto, F. (2012). Carbonyl sulfide (COS) as a tracer for canopy photosynthesis, transpiration, and stomatal conductance: Potential and limitations. *Plant, Cell, and Environment*, *35*(4), 657–667. https://doi.org/10.1111/j.1365-3040.2011.02451.x

Zhang, L., Davis, K. J., Schuh, A. E., Jacobson, A. R., Pal, S., Cui, Y. Y., et al. (2022). Multi-season evaluation of CO_2 weather in OCO-2 MIP models. *Journal of Geophysical Research: Atmospheres*, *127*(2), e2021JD035457. https://doi.org/10.1029/2021JD035457

Zumkehr, A., Hilton, T. W., Whelan, M., Smith, S., Kuai, L., Worden, J., & Campbell, J. E. (2018). Global gridded anthropogenic emissions inventory of carbonyl sulfide. *Atmospheric Environment*, *183*, 11–19. https://doi.org/10.1016/j.atmosenv.2018.03.063

Erratum

In the originally published version of this article, the Author Contributions list contained typographical errors. Jin Ma should be included under Conceptualization, Date curation, and Formal analysis. Marine Remaud should be included under Conceptualization, Data curation, Formal analysis, and Methodology and Writing – original draft. Maarten Kroll should be included under Formal analysis. Frédéric Chevallier should be included under Funding acquisition. The errors have been corrected, and this may be considered the authoritative version of record.